

# Electrolyte oxidation pathways in lithium-ion batteries

Bernardine L. D. Rinkel,<sup>1</sup> David S. Hall,<sup>1,2</sup> Israel Temprano,<sup>1</sup> Clare P. Grey<sup>1,2</sup>

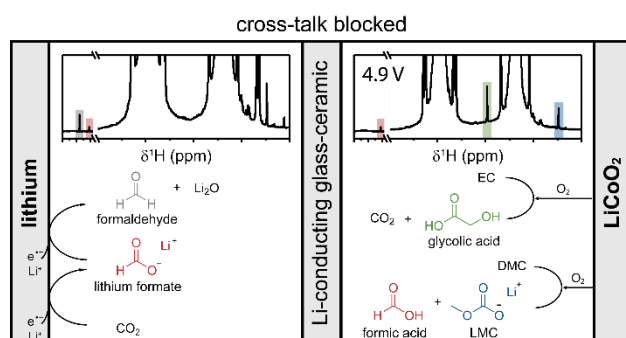
<sup>1</sup>Department of Chemistry, University of Cambridge, Cambridge UK

<sup>2</sup>The Faraday Institution, Harwell UK

## Abstract

The mitigation of decomposition reactions of lithium-ion battery electrolyte solutions is of critical importance in controlling device lifetime and performance. However, due to the complexity of the system, exacerbated by the diverse set of electrolyte compositions, electrode materials, and operating parameters, a clear understanding of the key chemical mechanisms remains elusive. In this work, operando pressure measurements, solution NMR, and electrochemical methods were combined to study electrolyte oxidation and reduction at multiple cell voltages. Two-compartment LiCoO<sub>2</sub>/Li cells were cycled with a lithium-ion conducting glass-ceramic separator so that the species formed at each electrode could be identified separately and further reactions of these species at the opposite electrode prevented. One principal finding is that chemical oxidation (with an onset voltage of ~4.7 V vs Li/Li<sup>+</sup> for LiCoO<sub>2</sub>), rather than electrochemical reaction, is the dominant decomposition process at the positive electrode surface in this system. This is ascribed to the well-known release of reactive oxygen at higher states-of-charge, indicating that reactions of the electrolyte at the positive electrode are intrinsically linked to surface reactivity of the active material. Soluble electrolyte decomposition products formed at both electrodes are characterised, and a detailed reaction scheme is constructed to rationalise the formation of the observed species. The insights on electrolyte decomposition through reactions with reactive oxygen species identified through this work have direct impact on understanding and mitigating degradation in high voltage/higher energy density LiCoO<sub>2</sub>-based cells, and more generally for cells containing nickel-containing cathode materials (e.g. LiNi<sub>x</sub>Mn<sub>y</sub>Co<sub>z</sub>O<sub>2</sub>; NMCs), as they lose oxygen at lower operating voltages.

## Table of content figure



## Introduction

A major challenge in lithium-ion battery (LIB) research is to find ways to improve energy density without compromising cell lifetime or safety. Many improvements have been made through optimisations of cell manufacturing and geometry,<sup>1</sup> although for further improvements as design limits are approached it becomes necessary to alter the cell chemistry or operating parameters. Two strategies that attract considerable industry and academic interest involve raising the upper cut-off voltage of the cell and increasing the nickel content in the positive electrode material (usually a layered transition metal oxide, *e.g.* LiCoO<sub>2</sub>; LCO or LiNi<sub>x</sub>Mn<sub>y</sub>Co<sub>z</sub>O<sub>2</sub>; NMC). A higher cut-off voltage allows for more Li<sup>+</sup>-ions to be extracted from the same mass of active material, due to the sloping voltage profile of these materials, and a higher nickel content allows for more Li<sup>+</sup>-ions to be extracted at a given voltage compared to NMC electrode with a lower nickel content.<sup>2</sup> However, going to a higher voltage, and thus to a higher state-of-charge (SOC), leads to rapid capacity fading, which limits the cycle life of the cell.<sup>3,4</sup> This is often ascribed to degradation at the positive electrode, including reconstruction of the surface layers and concomitant loss of lattice oxygen and transition metal dissolution, and decomposition of the electrolyte.<sup>5-8</sup>

LiCoO<sub>2</sub> remains the highest energy density cathode material and a commercially relevant cathode material for portable electronic devices, particularly mobile phones where energy density (rather than cost) is paramount. There is considerable industry and academic desire to increase the operational voltages to improve energy density for the development of so-called 'HV-LCO' cells (*i.e.* > 4.6 V vs. Li/Li<sup>+</sup>).<sup>9</sup> For example, a ~40% increase in energy density can be achieved by simply charging a LiCoO<sub>2</sub> cathode to 4.6 V vs Li/Li<sup>+</sup> rather than 4.3 V vs Li/Li<sup>+</sup>.<sup>10</sup> A major research focus involves modifying the cathode-electrolyte interface, for example with surface coatings and electrolyte additives.<sup>11,12</sup> Nonetheless, the chemical reactions and mechanisms at this interface are not well understood, posing a major hurdle for research efforts and for the rational design of electrolytes and electrolyte additives.

The direct and indirect consequences of electrolyte oxidation can negatively impact cell behaviour and lifetime in a variety of ways. The evolution of gaseous decomposition products can cause swelling or rupture of cell casings. Consumption of those evolved gases, deposition or further decomposition of the electrolyte decomposition products on either or both electrodes, as well as reactions of those species with the protective solid-electrolyte interphases (SEIs), and enhanced rates of transition metal dissolution can all lead to further irreversible capacity losses (as measured by electrode slippage) and slower interfacial kinetics (as measured by impedance).<sup>8,13-18</sup> These and other processes related to electrolyte oxidation lead to decreased cell performance and lifetime.

The observed decomposition of the electrolyte solution at high voltages is generally believed to proceed via oxidation of the organic carbonate solvent at the positive electrode. This has experimentally been shown to lead to the formation of CO<sub>2</sub>, CO, and H<sub>2</sub>O,<sup>3,19–21</sup> from *operando* measurements including differential electrochemical mass spectrometry (DEMS)<sup>20</sup> and online electrochemical mass spectrometry (OEMS).<sup>3,19,21–24</sup> Other studies have used *ex situ* measurements, such as analysing the electrolyte by gas chromatography mass spectrometry (GC-MS)<sup>25</sup> or nuclear magnetic resonance (NMR) spectroscopy<sup>26</sup> of the electrolyte, or X-ray photoelectron spectroscopy (XPS) of the electrodes<sup>27–30</sup> following cycling. There are also a variety of *in situ* and *operando* techniques that examine changes at the full cell level, for example isothermal microcalorimetry has been used to measure parasitic reaction rates and enthalpies<sup>2,31,32</sup> and differential thermal analysis (DTA) has been used to examine changes in salt concentration following cycling.<sup>33</sup> Finally, many additional decomposition reactions and products have been proposed based on *ab initio* calculations.<sup>34–36</sup> These studies provide valuable information about electrolyte decomposition, but it is difficult to conclusively identify individual reactions and chemical mechanisms.

It has been widely reported that electrolyte oxidation occurs electrochemically at the surface of both the active material and the conductive carbon particles.<sup>20,22</sup> There is evidence that the onset of Faradaic oxidation reactions only occurs at electrode potentials greater than ~4.8 vs Li/Li<sup>+</sup>, which is higher than to those expected in normal lithium-ion cell operation.<sup>37,38</sup> However, a wide range of electrode potentials for electrolyte decomposition have been reported in the literature.<sup>39</sup> It has also been suggested that electrolyte decomposition is related to the release of reactive oxygen species from the transition metal oxide lattice.<sup>40–44</sup> Recent work by Gasteiger and co-workers suggests that highly reactive lattice oxygen species are released as singlet oxygen into the electrolyte at high SOC that *chemically* oxidise the electrolyte.<sup>3,8,21,23</sup> This oxygen release occurs at lower electrode potentials than are required for Faradaic oxidation to occur and, thus, are suggested to be the dominant pathway for electrolyte oxidation in most lithium-ion cell designs. It is noteworthy that electrolyte oxidation and decomposition of the cathode material are intrinsically linked processes in this proposed mechanism. However, challenges remain to fully understand the chemical reactions that occur within cells. It would be valuable to develop a deeper understanding of chemical and electrochemical oxidation, for example by measuring their relative rates in a variety of cell chemistries or at different voltages. Furthermore, there is relatively limited understanding of the soluble decomposition products that are produced under various cell operating conditions.

A principal goal of the present work is to prepare a simplified, yet detailed summary of the myriad of processes that occur in support of a deeper understanding of how degradation occurs in a variety of cell designs and usage scenarios. The approach here adopted is to examine the wealth of published

results that have been reported in conjunction with a series of new experiments to bridge gaps and to answer specific questions in the literature. Generally, the chemical processes occurring at the SEI and in the electrolyte at the anode surface are better understood and have been reviewed,<sup>45</sup> whereas considerably less is known about the reactions at the cathode and the interplay between electrodes. In this work, the electrolyte decomposition products formed at each electrode individually were characterised by solution NMR spectroscopy and then used to infer the primary reactions that take place at each electrode. Separation of the electrolyte was achieved by using a lithium-ion conducting glass-ceramic separator, which prevents the migration of decomposition products in the electrolyte to the opposite electrode. This approach has been used previously by Gasteiger and colleagues to study gas-phase decomposition products, and it has been shown that with careful construction, the glass-ceramic is an effective barrier for cross-migration.<sup>19,22,23,46</sup>

First, the onset potential for electrolyte oxidation at the positive electrode was determined via operando pressure measurements. In situ gas volume measurements using polymer laminate pouch cells have shown that gas produced at low cell voltages is primarily due to SEI formation and reactions at the negative electrode, whereas the evolution of gas at high cell voltage correlates to electrolyte oxidation at the positive electrode.<sup>47</sup>

Subsequently, two LiCoO<sub>2</sub>/Li cells with a lithium-ion glass ceramic were cycled to below and above the onset potential for electrolyte oxidation, as determined from the operando gas experiment, and the electrolytes from both sides of the cell were analysed by solution NMR to identify any decomposition products that formed. Solution NMR spectroscopy was chosen as the main analytical method in this work because it provides considerable chemical and bonding information for several prominent elements in electrolyte solutions (H, C, F, P) and, although data interpretation is nuanced and often challenging, NMR is often suitable for the study of complex mixtures with low concentration components. The decomposition products observed in the LiCoO<sub>2</sub>/Li cells were compared with those formed through electrolysis of electrolyte, to gain insights into the oxidation mechanism (electrochemical or chemical oxidation). Finally, a unified reaction scheme is presented that considers primary processes at each electrode and secondary reactions that incorporate 'cross-talk' resulting from movement of gaseous products between electrodes.

## Experimental

### *Electrodes and electrolytes*

LiCoO<sub>2</sub> electrodes were prepared by grinding LiCoO<sub>2</sub> powder (Alfa Aesar, 99.5%, ~5 μm), Super P carbon nanoparticles (Timcal) and Kynar polyvinylidene difluoride (PVDF, Arkerma) in an 8:1:1 mass ratio with an agate mortar and pestle. *N*-methyl-2-pyrrolidone (NMP, Sigma-Aldrich, 99.5%, anhydrous) was added to form a slurry, which was blade-coated at a wet film thickness of 300 μm on an aluminium foil current collector. The films were dried at 65 °C in ambient atmosphere for 12 hours. Disks of the desired size were cut (active material loading of ~1 mg cm<sup>-2</sup>), dried further at 100 °C under vacuum for 24 hours, and then transferred to an argon-filled glovebox (MBraun, Germany; O<sub>2</sub> and H<sub>2</sub>O < 0.1 ppm). In all experiments, a 1.0 M LiPF<sub>6</sub> in ethylene carbonate (EC) and dimethyl carbonate (DMC) electrolyte (LP30; EC:DMC=50:50 (v/v), Sigma-Aldrich, battery grade) was used.

### *Two-compartment cells*

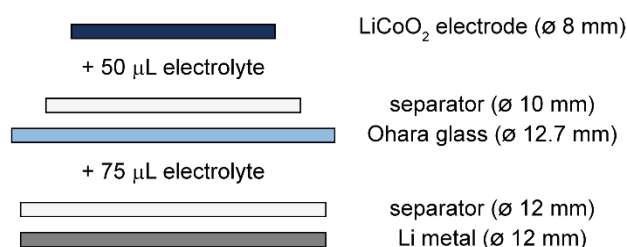
LiCoO<sub>2</sub>/Li cells were assembled in a two-compartment half-inch inner-diameter Swagelok cell as shown in Figure 1a. A lithium-ion conducting glass-ceramic (Ohara, Japan) was placed between two borosilicate glass fibre separators (Whatmann, GF/B, 0.68 mm thick, 1.0 μm pore size), so that the species formed at each electrode could be identified separately and so further reactions of these species at the opposite electrode are prevented. To further prevent mixing of the electrolytes, the electrodes and separators were punched to smaller diameters than the glass-ceramic, the separators were wetted with only the minimal amount of electrolyte, and the cells were kept upright to prevent leakage of the electrolyte around the edges of the glass-ceramic. The LiCoO<sub>2</sub>/Li cells were assembled as follows: a lithium metal foil disk (Ø 12 mm; Aldrich, 99%) was placed on the anode current collector at the base of the cell, covered with a borosilicate glass fibre separator (Ø 12 mm) and wetted with 75 μL of electrolyte. The glass-ceramic (Ø 12.7 mm) was then carefully placed and gently pressed onto the separator, to ensure good contact between with the glass fibre separator and the ceramic. Another, slightly smaller, glass fibre separator (Ø 10 mm) was placed in the centre of the glass-ceramic and wetted with 50 μL of electrolyte and a LiCoO<sub>2</sub> electrode (Ø 8 mm) was placed on top. A cathode current collector/plunger was added to seal the cell, which was then gently tightened to avoid breaking the brittle glass-ceramic. All cell assembly was performed in an argon-filled glovebox.

### *Electrochemical measurements*

Electrochemical measurements were performed using a Biologic MPG2 potentiostat/galvanostat instrument running EC-lab software. The LiCoO<sub>2</sub>/Li cells were galvanostatically charged and discharged

at C/5 (based on the practical capacity of  $\text{LiCoO}_2 = 140 \text{ mAh g}^{-1}$ ) between 3.0–4.6 V or 3.0–4.9 V (vs  $\text{Li/Li}^+$ ) for 10 cycles.

**a) half-inch Swagelok cell**



**b) one-inch Swagelok cell**

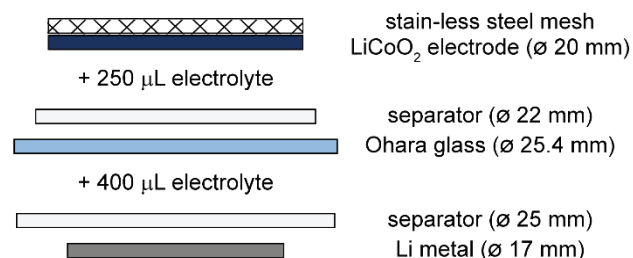


Figure 1. Schematic illustration of the assembly of the a) half-inch and b) one-inch two-compartment electrochemical cells with a lithium-ion conducting glass ceramic (Ohara glass) between two porous borosilicate glass fibre separators.

### Operando pressure measurements

The onset potential for gas evolution at the cathode was determined by measuring the internal cell pressure as a function of the voltage. A two-compartment setup with a lithium-ion conducting glass-ceramic was used to inhibit cross-migration of species between the electrode compartments.  $\text{LiCoO}_2/\text{Li}$  cells were assembled in a two-compartment one-inch Swagelok cell, in a similar way as described above, except larger electrodes ( $\varnothing 17 \text{ mm}$  lithium metal foil disk and  $\varnothing 20 \text{ mm}$   $\text{LiCoO}_2$  electrode), separators ( $\varnothing 25$  and  $20 \text{ mm}$ ) and more electrolyte ( $400 \mu\text{L}$  for the anode and  $250 \mu\text{L}$  for the cathode) were used in the one-inch Swagelok setup (Figure 1b). A stainless-steel mesh was placed on top of the  $\text{LiCoO}_2$  electrode to ensure electrical contact between the cathode and lithium metal anode, while simultaneously allowing for any formed gases to diffuse into the headspace.

The Swagelok cell was connected to an Omega (PX309-030A5V) pressure sensor to measure changes in the internal pressure of the cell. After a 12-hour rest at open circuit voltage (OCV) to allow the baseline pressure to stabilise, the cell was charged to a series of target voltages in steps of 0.1 V and ranging from 4.2 V to 5.0 V. For each cut-off voltage, the cell was first charged at C/5, held at the target voltage for 10 hours, and then allowed to rest at open circuit for one hour. This series was then repeated for each target voltage in the series. The measurements were performed at 25 °C in a temperature-controlled environment.

### Electrolysis of electrolyte (H-cell experiments)

An H-cell was used to electrolyse the electrolyte, so that the species formed through electrochemical oxidation could be compared to the degradation products formed inside the  $\text{LiCoO}_2/\text{Li}$  cells. A glass H-cell with two compartments separated by three separators (Celgard 2400), in order to limit convective mixing between the two halves, was filled with 6 mL of electrolyte (LP30; 1 M  $\text{LiPF}_6$  in EC:DMC=50:50

(v/v) in each compartment. A Pt wire (working electrode, 5 cm) and a Ag/AgCl (saturated KCl in acetonitrile) electrode (reference electrode) were placed in one half and a stainless-steel mesh (counter electrode, approx. 2 cm × 6 cm) was placed in the other (Figure S 1). The H-cell components were dried for several hours at 60 °C and transferred while still hot into an argon-filled glovebox, where all assembly and electrochemical measurements were performed. Each compartment was covered with parafilm to prevent evaporation of the electrolyte. Electrochemical measurements were conducted using a Biologic SP-150 potentiostat/galvanostat. A current of 10 mA was applied for 30 minutes (i.e., 5 mAh), after which 0.1 mL of electrolyte was taken from each side to be analysed by solution NMR.

After 30 min electrolysis, the level of fluid in the positive electrode compartment was observed to have decreased by about a third (~2 mL) while the level of fluid in the negative electrode compartment was observed to have risen by the same amount.

#### *Electrolyte hydrolysis*

To understand what electrolyte decomposition products form through the hydrolysis of the electrolyte solution, LP30 electrolyte (1 M LiPF<sub>6</sub> in EC:DMC =50:50 v/v) was prepared with 10% water (v/v %) and stored for 2 months in an air-tight polypropylene container. A control electrolyte was stored under the same conditions and 0.1 mL was taken from each electrolyte solution for characterisation by solution NMR.

#### *Solution NMR*

After cycling the LiCoO<sub>2</sub>/Li cells, the cells were disassembled in an argon-filled glovebox and the glass fibre separator was soaked in 0.7 mL of DMSO-d<sub>6</sub> (Aldrich, 99.9 atom % D, 99% CP) for 5 minutes. The solution was transferred to an airtight NMR tube fitted with a Young's tap.

One-dimensional <sup>1</sup>H, <sup>19</sup>F{<sup>1</sup>H}, <sup>31</sup>P{<sup>1</sup>H} NMR spectra and two-dimensional <sup>1</sup>H–<sup>1</sup>H correlation spectroscopy (COSY) and <sup>1</sup>H–<sup>13</sup>C heteronuclear single quantum coherence (HSQC) NMR spectra were recorded on a Bruker AVANCE III HD 11.7 T (ω<sub>1H</sub> = 500 MHz) spectrometer using a BBO probe. <sup>1</sup>H and <sup>13</sup>C spectra were internally referenced to DMSO-d<sub>6</sub> at 2.50 ppm (δ <sup>1</sup>H) and 39.5 ppm (δ <sup>13</sup>C), <sup>19</sup>F and <sup>31</sup>P spectra were internally referenced to LiPF<sub>6</sub> at –74.5 ppm (δ <sup>19</sup>F) and –145.0 ppm (δ <sup>31</sup>P).

## Results

*Two-compartment cells:*

### **Operando pressure measurement (1<sup>st</sup> charge):**

A LiCoO<sub>2</sub>/Li half-cell was charged while measuring the internal pressure of the cell, Figure 2 showing the time-dependent *operando* pressure data overlaid with the cell voltage. The cell pressure decreases slightly as the cell was charged up to 4.6 V, but between 4.6 – 4.7 V the pressure starts to rise noticeably, and keeps increasing as the cell was charged up to 4.9 V. The increase in cell pressure at high voltages (> 4.6 V) is attributed to the evolution of gaseous decomposition products at the positive electrode, which increases at higher voltages. The small decrease in cell pressure at low voltages is most likely due to a slow leakage of gases from the cell. The gas evolution from electrolyte decomposition at the negative (Li) electrode is assumed to be similar throughout the experiment and therefore does not explain the increase in cell pressure at the end of charge: Even though the lithium metal surface becomes passivated with an SEI through the reduction of electrolyte when the cell is assembled, as the cell is charged, lithium ions are extracted from the positive electrode and plated (*i.e.*, reduced) as microstructural lithium metal on the surface of the negative electrode, continuously providing a fresh surface for electrolyte reduction and thus giving a constant evolution of gases throughout the experiment. Conversely, the reduction of any CO<sub>2</sub> that is formed may cause a slow decrease in pressure.<sup>17</sup> The two-compartment setup in this work should inhibit any migration of non-gaseous electrolyte oxidation species to the negative electrode.

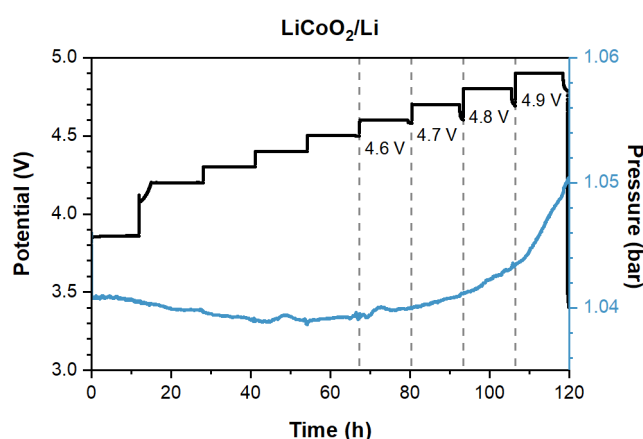


Figure 2. Operando pressure measurement of a LiCoO<sub>2</sub>/Li cell charged in 0.1 V steps from OCV to 5.0 V (for detailed charging protocol, see Methods section). The internal cell pressure and voltage-time data are shown in blue and black, respectively. The electrolyte was a 1M LiPF<sub>6</sub> solution in 1:1 EC:DMC (LP30). The electrodes were separated by a lithium-conducting glass-ceramic to prevent migration of any decomposition species across the cell.

### **Electrochemistry (cycling data):**

Two LiCoO<sub>2</sub>/Li cells were constructed and cycled to just below (4.6 V) or well above (4.9 V) the onset voltage for electrolyte oxidation as determined by the *operando* pressure measurement. Similar to

the setup used for the *operando* pressure measurement, a lithium-conducting glass-ceramic was used to separate the cell compartments to allow for the separate identification of the electrolyte decomposition products formed at each electrode. This had the further effect of preventing any 'cross-talk' reactions by preventing migration of the dissolved species in the electrolyte to the opposite electrode. Two LiCoO<sub>2</sub>/Li cells were cycled between 3.0 – 4.6 or 3.0 – 4.9 V at a C/5 rate for 10 cycles (electrochemical data is shown in the Supplementary Information; Figure S 2). The cell cycled to 4.6 V showed some capacity loss (17%) over the 10 cycles (Figure S 2a), which is attributed degradation processes at the positive electrode, including reconstruction of the surface layers and concomitant loss of lattice oxygen, and decomposition of the electrolyte as well as phase transformations involving a change in the stacking sequence of the material<sup>48</sup>, all resulting in impedance growth at the surface of the LiCoO<sub>2</sub> particles.<sup>49</sup> The cell cycled to 4.9 V suffered from a far more dramatic decrease in capacity (99% capacity loss; Figure S 2b), which may correspond to an enhanced rate of degradation processes at higher voltages. After cycling, the two LiCoO<sub>2</sub>/Li cells were disassembled, and the glass fibre separators were soaked in deuterated DMSO to extract the electrolyte and its decomposition products for analysis by solution NMR.

#### *Solution-state NMR:*

Each of the four extracted samples (electrolytes from the positive and negative electrode, cycled from 3.0 V to 4.6 or 4.9 V), as well as a pristine reference sample, was characterised using <sup>1</sup>H, <sup>19</sup>F, and <sup>31</sup>P one and two-dimensional homo and heteronuclear NMR spectroscopies. A list of the observed signals in the <sup>1</sup>H, <sup>19</sup>F and <sup>31</sup>P NMR spectra (Table S 3) as well as a detailed discussion of their assignments are given in the SI. Briefly, the assignments of the NMR signals are supported by complementary and detailed NMR measurements such as two-dimensional experiments (COSY and HSQC) and J-coupling analysis, measurements of reference compounds reference compound measurements, and literature examples. An overview of the assignments of the observed chemical shifts is given in Table 1 and summarised below.

#### **<sup>1</sup>H NMR**

Figure 3 shows the <sup>1</sup>H NMR spectra of the pristine electrolyte (bottom) and the electrolyte extracted from the cells cycled from 3.0 V to 4.6 V (middle) and 4.9 V (top). The <sup>1</sup>H NMR spectra over the full shift range (12 – 0 ppm) are given in the supplementary information (Figure S 4). It is immediately observed that the spectra contain several differences in the weak signals arising from minor components between the two sides of each cell, suggesting that the glass-ceramic successfully inhibited cross-migration of species other than lithium ions.

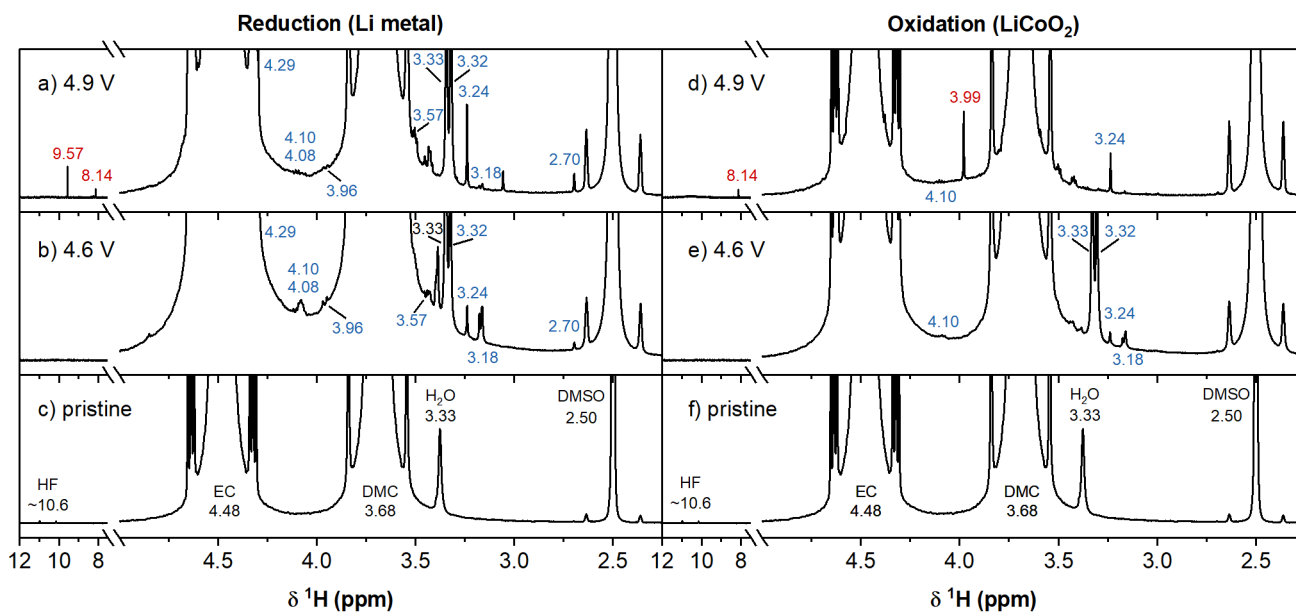


Figure 3.  $^1\text{H}$  solution NMR spectra of LP30 electrolyte extracted from the two-compartment  $\text{LiCoO}_2/\text{Li}$  cells after 10 cycles between 3.0 – 4.9 V (top; a, d) and 3.0 – 4.6 V (middle; b, e) and pristine electrolyte (bottom; c, f). The spectra on the left are of electrolyte from the lithium metal side (a, b), the spectra on the right are of electrolyte from the  $\text{LiCoO}_2$  side of the cell (d, e). The signals of ethylene carbonate (EC; 4.48 ppm), dimethyl carbonate (DMC; 3.68 ppm) and dimethyl sulfoxide (DMSO; 2.50 ppm) are annotated in black on the bottom spectra. The chemical shifts in blue and red correspond to signals that appeared after cycling to 4.6 V and 4.9 V, respectively.

**Pristine electrolyte:** The  $^1\text{H}$  NMR spectrum of the pristine electrolyte (Figure 3c and f) shows two main signals of ethylene carbonate (EC; 4.48 ppm) and dimethyl carbonate (DMC; 3.68 ppm).<sup>50,51</sup> As expected, these solvent peaks are present in all of the spectra in Figure 3. Traces of hydrofluoric acid (HF) and water are also detected by the appearance of signals at 10.6 ppm (HF) and 3.33 ppm ( $\text{H}_2\text{O}$ ).<sup>52–54</sup> The signal at 2.50 ppm is assigned to non-deuterated DMSO impurities in the  $\text{DMSO-d}_6$  solvent.<sup>52</sup>

**4.6 V:** After cycling to 4.6 V, several new signals appear between 2.5 – 5 ppm in the  $^1\text{H}$  NMR spectrum of the electrolytes from both the positive and negative electrolyte, indicating the formation of electrolyte decomposition products. At the  $\text{LiCoO}_2$  side (Figure 3d), the electrolyte contains methanol (4.10, 3.18 ppm),<sup>52</sup> lithium methoxide (3.32 ppm) and lithium methyl carbonate (LMC; 3.24 ppm).<sup>55</sup> At the lithium metal side (Figure 3c), the  $^1\text{H}$  NMR spectrum of the electrolyte also shows the species observed at the positive electrode, but additionally contains, lithium ethylene dicarbonate (LEDC; 4.29 ppm),<sup>56</sup> lithium ethylene monocarbonate (LEMC; 4.08 and 3.55 ppm), the difluorophosphate ester,  $\text{OPF}_2(\text{OCH}_3)$  (3.96 ppm) and a signal tentatively ascribed lithium succinate (2.70 ppm).

**4.9 V:** After cycling to 4.9 V, additional signals between 8 – 11 ppm appear in the electrolytes of both electrodes. The  $^1\text{H}$  spectrum of the electrolyte from the  $\text{LiCoO}_2$  side cycled to 4.9 V (Figure 3b) shows the additional presence of formic acid (8.14 ppm),<sup>57</sup> HF and other H-bonded protons (broad signal at 10.6 ppm; Figure S 12) and lithium glycolate or glycolic acid (3.99 ppm). No trace moisture remains in the electrolyte, as the signal at 3.33 ppm is no longer observed. The  $^1\text{H}$  spectrum of the electrolyte

from the lithium metal side of the cell cycled to 4.9 V (Figure 3a) shows two additional signals compared to the  $^1\text{H}$  NMR spectrum of the 4.6 V cell, assigned to formaldehyde (9.57 ppm) and lithium formate (8.14 ppm).<sup>57</sup>

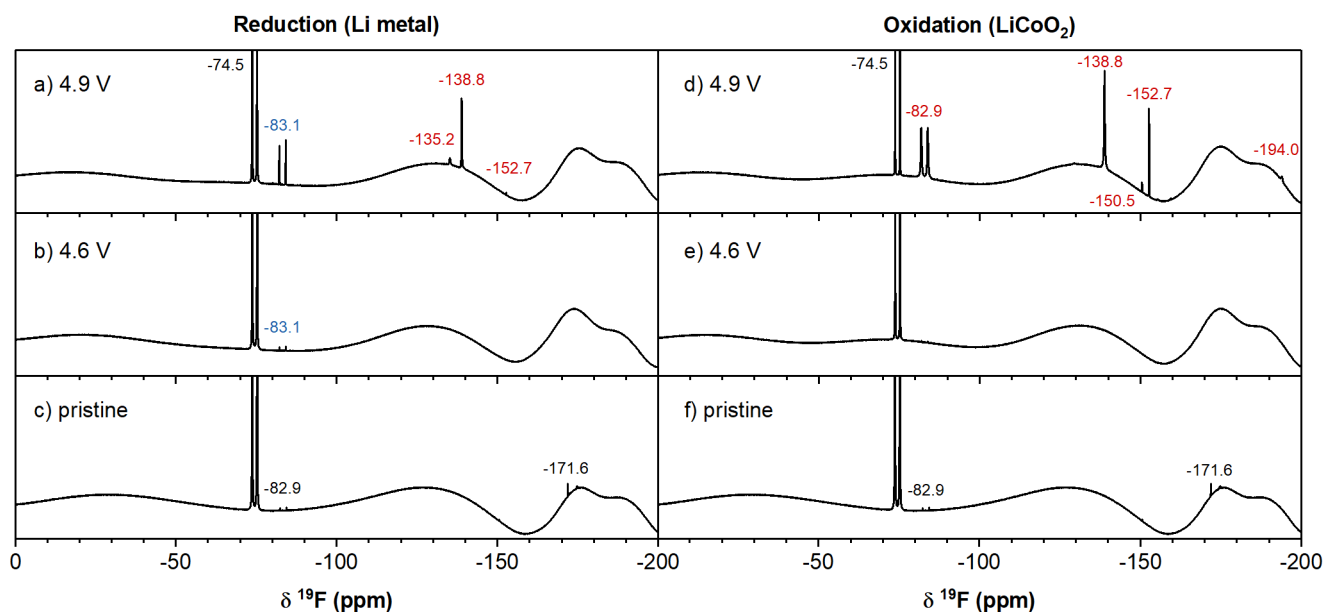


Figure 4.  $^{19}\text{F}\{^1\text{H}\}$  solution NMR spectra of LP30 electrolyte extracted from the two-compartment  $\text{LiCoO}_2/\text{Li}$  cells after 10 cycles between 3.0–4.9 V (top; a, d) and 3.0–4.6 V (middle; b, e) and pristine electrolyte (bottom; c, f). The spectra on the left are of electrolyte from the lithium metal side (a, b), the spectra on the right are of electrolyte from the  $\text{LiCoO}_2$  side of the cell (d, e). The chemical shifts of the signals found in the pristine electrolyte are given in black, those of signals that appeared after cycling to 4.6 and 4.9 V are given in blue and red, respectively. The extremely broad features at approximately -130 ppm and -175 and -190 ppm arise from a combination of probe background and ringing effects and are not due to additional electrolyte species.

### $^{19}\text{F}$ NMR

**Pristine electrolyte:** The  $^{19}\text{F}\{^1\text{H}\}$  spectrum measured from the pristine electrolyte (Figure 4c and f) shows a major signal from  $\text{LiPF}_6$  (–74.5 ppm,  $d, {}^1J_{\text{P-F}} = 710$  Hz, see Figure S11 for the  $^{31}\text{P}$  NMR spectrum), and minor signals from  $\text{LiPO}_2\text{F}_2$  (–82.9 ppm,  $d, {}^1J_{\text{P-F}} = 955$  Hz) and HF (–171.6 ppm) impurities.<sup>51,53,54</sup>

**4.6 V:** The  $^{19}\text{F}$  NMR spectrum of the electrolyte from the  $\text{LiCoO}_2$  side (Figure 4e) reveals no detectable fluorine-based decomposition products. The electrolyte take from the lithium metal side after cycling to 4.6 V (Figure 4b), however, shows the presence of  $\text{OPF}_2(\text{OCH}_3)$  (–83.1,  $d, {}^1J_{\text{P-F}} = 947$  Hz).

**4.9 V:** After cycling to the higher cut-off voltage of 4.9 V, several new signals are observed in the spectra measured from the electrolytes from both sides of the cell. At the  $\text{LiCoO}_2$  side (Figure 4b), the presence of  $\text{OPF}_2(\text{OH})/\text{PO}_2\text{F}_2^-$  (–82.9 ppm, see Figure S 11 for the  $^{31}\text{P}$  NMR spectrum), silicon fluorides ( $\text{SiF}_x$ ,  $x = 4-6$ ; –138.8),<sup>58</sup> lithium fluoroborate ( $\text{LiBF}_4/\text{BF}_4^-$ ; –152.7 ppm; Figure S 15)<sup>59</sup> and HF (–194.0 ppm)<sup>53,54</sup> are observed. A signal at -150.5 ppm is tentatively assigned to  $\text{OPF}_2(\text{OH})-\text{BF}_3$ .<sup>60</sup> In the lithium metal electrolyte (Figure 4a), a higher concentration of  $\text{OPF}_2(\text{OCH}_3)$  is seen, as well as signals from silicon fluoride species (–135.2 and –138.8 ppm)<sup>58</sup> and  $\text{LiBF}_4$  or  $\text{BF}_4^-$  (–152.7 ppm).

Table 1. Summary of observed chemical shifts and the corresponding species assignments in this work. It is noted that not all species in this table are expected in commercial lithium-ion cells, which may use different separators and additives.

Nucleus	Chemical shift (ppm)	Assignment
$^1\text{H}$	4.48 (s)	Ethylene carbonate (EC)
	3.69 (s)	Dimethyl carbonate (DMC)
	~10.6 (d, $^1J_{\text{F-H}} = 410$ Hz; broad)	Hydrofluoric acid (HF)
	9.61 (s)	Glyoxal
	9.57 (s)	Formaldehyde
	8.14 (s)	Formic acid
	7.71 (s)	Vinylene carbonate (VC)
	6.55 (ddd, $^2J_{\text{F-H}} = 60.7$ Hz; $^3J_{\text{H-H}} = 4.1, 0.7$ Hz); 4.73 (ddd, $^2J_{\text{F-H}} = 36.3$ Hz; $^3J_{\text{H-H}} = 11.0, 4.2$ Hz); 4.64 (ddd, $^2J_{\text{F-H}} = 21.3$ Hz; $^3J_{\text{H-H}} = 11.0, 0.7$ Hz)	Fluoroethylene carbonate (FEC)
	5.79 (s) 5.70 (s) 5.69 (s)	Acetal; $\text{RCH}(\text{OR})_2$ (e.g. methanediol, methoxymethanol)
	4.29 (s)	Lithium ethylene dicarbonate (LEDC)
	4.10 (q, $^3J_{\text{H-H}} = 5.5$ Hz); 3.18 (d, $^3J_{\text{H-H}} = 5.5$ Hz)	Methanol
	4.08 (t, $^3J_{\text{H-H}} = 4.7$ Hz); 3.55 (t, $^3J_{\text{H-H}} = 4.7$ Hz)	Lithium ethylene monocarbonate (LEMC)
	3.99 (s)	Glycolic acid or lithium glycolate
	3.96 (d, $^3J_{\text{P-H}} = 10.0$ Hz)	$\text{OPF}_2(\text{OCH}_3)$
	3.34 (s)	$\text{H}_2\text{O}$
	3.32 (s)	Lithium methoxide ( $\text{LiOCH}_3$ )
	3.24 (s)	Lithium methyl carbonate (LMC)
2.70 (s)	Lithium succinate	
$^{19}\text{F}\{^1\text{H}\}$	-65.9 (dd, $^1J_{\text{P-F}} = 762$ Hz, $^2J_{\text{F-F}} = 56$ Hz); -81.0 (dt, $^1J_{\text{P-F}} = 740$ Hz, $^2J_{\text{F-F}} = 60$ Hz)	Trifluorooxalatophosphate ( $\text{PF}_3(\text{C}_2\text{O}_4)$ )
	-74.5 (d, $^1J_{\text{P-F}} = 710$ Hz)	$\text{LiPF}_6$
	-82.9 (d, $^1J_{\text{P-F}} = 955$ Hz)	$\text{OPF}_2(\text{OH})$
	-83.1 (d, $^1J_{\text{P-F}} = 947$ Hz)	$\text{OPF}_2(\text{OCH}_3)$
	-126.3 (s)	Fluoroethylene carbonate (FEC)
	-135.2 (s) -138.8 (s)	Silicon fluorides ( $\text{SiF}_x$ )
	-150.5 (s)	$\text{OPF}_2(\text{OH})\text{-BF}_3$
	-152.7 (s)	$\text{BF}_4^-$
	-171.6 (s) -194.0 (s)	HF (in various coordinations and complexations, e.g. $\text{FHF}^-$ , $\text{F}(\text{HF})_2$ , $\text{F}(\text{HF})_3$ or $\text{F}(\text{HF})_4$ )
	$^{31}\text{P}$	-145.0 (septet, $^1J_{\text{F-P}} = 711$ Hz)
-16.6 (t, $^1J_{\text{F-P}} = 947$ Hz)		$\text{OPF}_2(\text{OCH}_3)$
-15.5 (t, $^1J_{\text{F-P}} = 955$ Hz)		$\text{OPF}_2(\text{OH})$

### Electrochemical oxidation of electrolyte (Electrolytic H-cell experiments)

To consider whether any of the electrolyte decomposition products identified in the  $\text{LiCoO}_2/\text{Li}$  cells formed via *electrochemical* oxidation, a conventional 2-compartment electrolysis H-cell was constructed. Three separators were used to partition the cell in order to limit convective mixing

between the two halves. A noticeable volume displacement from the positive electrode compartment to the negative electrode compartment was observed: after 30 min electrolysis, the level of fluid in the positive electrode compartment was observed to have decreased by about a third (~2 mL) while the level of fluid in the negative electrode compartment was observed to have risen by the same amount. This net movement of the solution ascribed to the establishment of an electro-osmotic flow, generally defined as the motion of a fluid in response to an external electric field across a porous material, capillary tube, membrane, or other fluid conduit.<sup>61,62</sup> The phenomenon is well-known for aqueous systems, for example across ion-exchange membranes in fuel cells and electrolyzers,<sup>63</sup> through plant phloem and across membranes in vascular biology,<sup>64</sup> and through silica capillaries in capillary electrophoresis separations.<sup>65</sup> However, the authors are not aware of any rigorous treatment of electro-osmosis of non-aqueous electrolyte solutions across nonpolar, porous polymer battery separators. We therefore suggest this phenomenon may have significance for the operation of high power and fast-charging batteries that merits its own investigation. With regards to the present work, the practical result of the observed volume displacement is that it will have prevented the migration of any reduction species from the negative electrode to the positive electrode compartment of the H-cell.

Figure 5 shows the <sup>1</sup>H NMR spectrum measured from the electrochemically oxidised electrolyte (d). For comparison, the results from the two-compartment LiCoO<sub>2</sub>/Li cells cycled to 4.9 V (e) and pristine electrolyte (f) are also shown. A peak corresponding to acetonitrile ( $\delta$  <sup>1</sup>H = 2.07 ppm) is not observed for any of the spectra, indicating that there was no leakage from the reference electrode into the cell. Electrochemical oxidation of the electrolyte leads to a large range of new signals, but most of the carbonate solvent remains intact. By repeating the experiment using an electrolyte without EC (*i.e.* 1M LiPF<sub>6</sub> in DMC), the signals corresponding to the electrolyte decomposition products originating from EC and DMC can be separated (Figure S 16). A list of the observed signals in the <sup>1</sup>H, <sup>19</sup>F and <sup>31</sup>P NMR spectra (Table S 3) as well as a detailed discussion of their assignments are given in the SI.

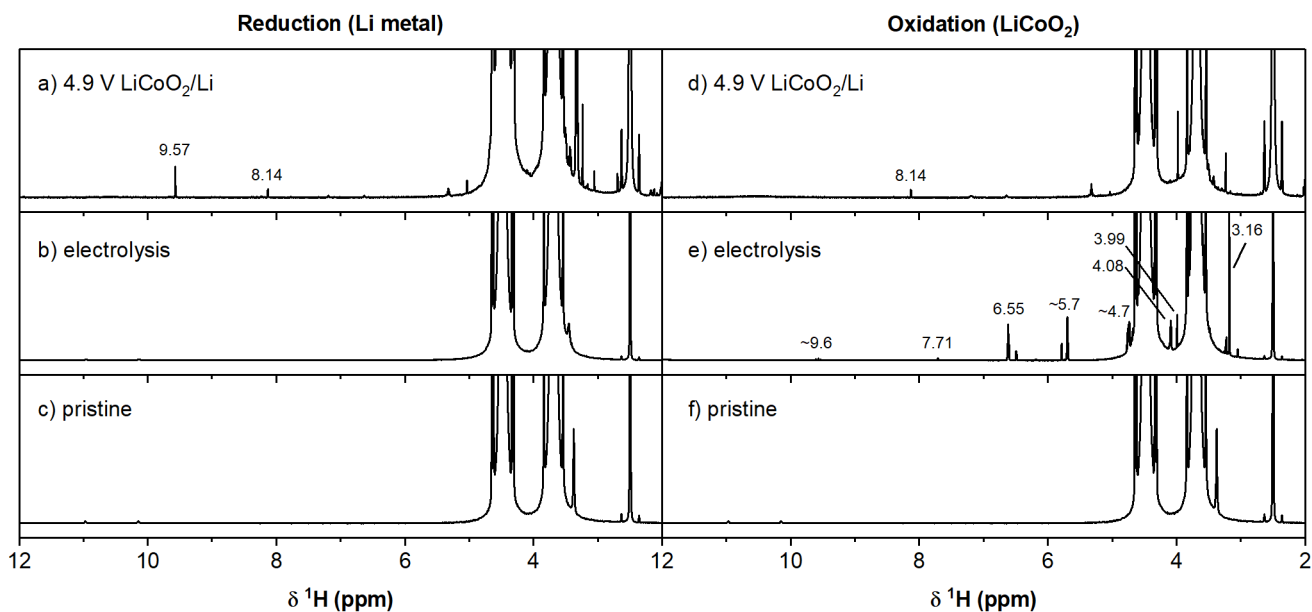


Figure 5.  $^1\text{H}$  solution NMR spectra of LP30 electrolyte extracted from the two-compartment  $\text{LiCoO}_2/\text{Li}$  cells after 10 cycles between 3.0 – 4.9 V (top; a, d) and the conventional 2-compartment electrolysis H-cell after applying a current of 10 mA for 30 min (middle; b, e) and pristine electrolyte (bottom; c, f).

**$^1\text{H}$  NMR:** The signals attributed to EC decomposition products are assigned to vinylene carbonate (VC; 7.71 ppm),<sup>66</sup> a small symmetrical molecule with an aldehyde-functionality, such as glyoxal,  $\text{H}-\text{C}(=\text{O})-\text{C}(=\text{O})-\text{H}$  (9.61 ppm) and fluoroethylene carbonate (FEC; 6.55, 4.73, 4.64 ppm, see Figure S 17). The signals originating from the decomposition products of DMC are attributed to formaldehyde (9.57 ppm), glycolic acid or lithium glycolate (3.99 ppm) various simple acetal species,  $\text{RCH}(\text{OR})_2$ , such as methanediol and methoxymethanol (5.79 ppm, s; 5.70 ppm, s; 5.69 ppm, s). Finally, a broad signal at  $\sim 12.4$  ppm is observed and assigned to H-bonded protons in the electrolyte.

**$^{19}\text{F}$  NMR:** The  $^{19}\text{F}$  NMR spectrum of the electrochemically oxidised electrolyte (Figure S 18) is dominated by the signal from the  $\text{LiPF}_6$  salt (-74.5 ppm), but reveals new signals from  $\text{OPF}_2\text{OH}/\text{PO}_2\text{F}_2^-$  (-83.6 ppm), FEC (-126.3 ppm, Figure S 19),  $\text{LiBF}_4/\text{BF}_4^-$  (-153.0 ppm) and HF (-172.8 ppm). The multiplets at -65.9 and -81.0 ppm are tentatively assigned to trifluorooxalatophosphate ( $\text{PF}_3\text{C}_2\text{O}_4$ ).

The electrolyte decomposition products identified in the various experiments in this work are summarised in Table 2.

Table 2. Summary of electrolyte decomposition products observed in this work, as identified by solution NMR, and the conditions under which they are formed. A 'x' indicates the species was present under that condition, whereas a '-' indicates the species was not.

Species	Pristine electrolyte	Lithium metal		LiCoO <sub>2</sub> electrode		Electrochemical electrolyte oxidation
		4.6 V	4.9 V	4.6 V	4.9 V	
H <sub>2</sub> O	x	x	x	x	-	-
HF	x	-	-	-	x	x
Lithium ethylene dicarbonate (LEDC)	-	x	x	-	-	-

Lithium methyl carbonate (LMC)	-	X	X	X	X	X
Lithium methoxide	-	X	X	X	-	-
Lithium succinate	-	X	X	-	-	-
Methanol	-	X	X	X	X	X
Formic acid	-	-	X	-	X	-
Formaldehyde	-	-	X	-	-	X
Glycolic acid/lithium glycolate	-	-	-	-	X	X
Glyoxal	-	-	-	-	-	X
Vinylene carbonate (VC)	-	-	-	-	-	X
Fluoroethylene carbonate (FEC)	-	-	-	-	-	X
Acetals	-	-	-	-	-	X
OPF <sub>2</sub> (OH)	-	-	-	-	X	X
OPF <sub>2</sub> (OCH <sub>3</sub> )	-	X	X	-	-	-
PF <sub>3</sub> (C <sub>2</sub> O <sub>4</sub> )	-	-	-	-	-	X
SiF <sub>x</sub>	-	-	X	-	X	-
BF <sub>4</sub> <sup>-</sup>	-	-	X	-	X	X
OPF <sub>2</sub> OH-BF <sub>3</sub>	-	-	-	-	X	-

## Discussion

The results of this work were used to construct a detailed scheme showing the various electrolyte decomposition reactions that occur at high voltages/SOC, which are summarised here to put the following discussion in context (Figure 6). The scheme is based on both a careful analysis of the NMR spectra collected in this work and from a review of the wealth of proposed reactions in the extensive published literature. Electrolyte decomposition pathways were categorised into three types of reactions:

- 1) Chemical reduction and oxidation
- 2) Faradaic reduction and oxidation
- 3) Non-redox reactions

We were careful to adhere to the fundamentals of organic and inorganic chemical reaction mechanisms,<sup>67,68</sup> and to be consistent with known data. The following discussion walks through the logic and organic reactions used to construct Figure 6. We then summarise the reactions and discuss the broader implications of the proposed mechanisms.

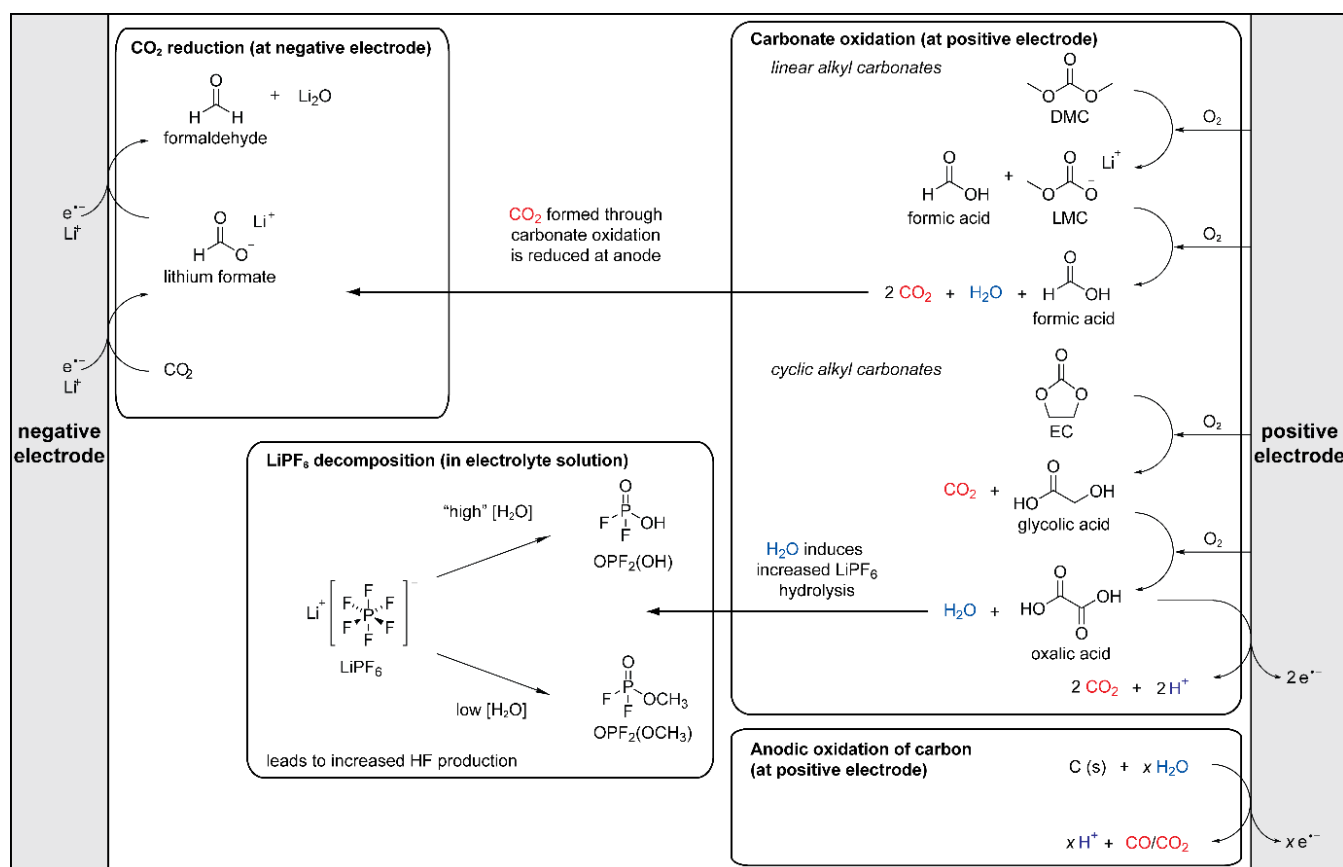


Figure 6. Overview of electrolyte decomposition reactions that occur at high voltages (or high SOC) initiated at the positive electrode.

### *Electrochemical (Faradaic) versus chemical (non-Faradaic) oxidation of electrolyte*

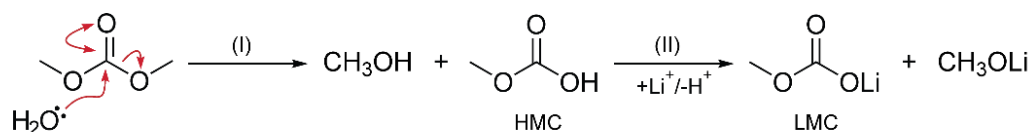
The main products formed through electrochemical oxidation of the electrolyte (in the H-cell and on a Pt electrode) were identified as fluoroethylene carbonate (FEC), vinylene carbonate (VC), formaldehyde and acetal species, whereas the main products found on the LiCoO<sub>2</sub> side of the two-compartment LiCoO<sub>2</sub>/Li cells were formic acid, glycolic acid or lithium glycolate and lithium methyl carbonate (LMC; Table 2). The oxidation-decomposition species resulting from electrochemical oxidation are clearly very different from those observed in the LiCoO<sub>2</sub>/Li cells, implying that electrochemical oxidation is not the dominant oxidation mechanism at the LiCoO<sub>2</sub> or carbon surface during cycling up to cell voltages as high as 4.9 V (vs Li/Li<sup>+</sup>). This indicates that they must originate from chemical oxidation of the electrolyte, presumably via mechanism involving oxygen evolved from the cathode surface as previously suggested by Gasteiger and co-workers.<sup>3,8,21,23</sup>

### *Carbonate solvent oxidation at the positive electrode*

The LiCoO<sub>2</sub>/Li cell cycled to 4.6 V operates below the gas evolution onset potential (4.7 V vs Li/Li<sup>+</sup>), therefore no significant electrochemically-driven electrolyte decomposition is expected to occur at the LiCoO<sub>2</sub> electrode. The observed electrolyte decomposition products on the LiCoO<sub>2</sub> side at 4.6 V are lithium methyl carbonate (LMC), lithium methoxide and methanol (Table 2). These products were also observed in the electrolyte that was stored in a polypropylene container for two months both with the addition of water (10,000 ppm) and without (see supplementary information). Thus, the formation of small quantities of methanol, lithium methoxide and LMC at the positive electrodes at voltages below the gas-onset voltage are proposed to occur largely through the hydrolysis of DMC with trace moisture in the electrolyte. Scheme 1 shows a general hydrolysis pathway of DMC, although it may in fact be acid-catalysed by H<sup>+</sup> and/or PF<sub>5</sub> at the carbonyl group. Notably, no evidence for the hydrolysis of EC is observed (*i.e.* there is an absence of lithium ethylene monocarbonate; LEMC, or ethylene glycol; EG), which could imply EC is less susceptible to hydrolysis and/or that the concentration of EC hydrolysis products in the electrolyte was below the detection limit.

*Scheme 1. The acid-driven hydrolysis reaction of dimethyl carbonate (DMC) to form lithium methyl carbonate (LMC) and methanol.*

Hydrolysis of DMC



In the electrolyte solution, any protic species formed (*e.g.*, methanol or hydrogen methyl carbonate; HMC) may exist as the protic acid, as the lithium conjugate base complex (in this case, lithium

methoxide and LMC; Scheme 1, step II) or as the uncoordinated conjugate base. The preferred “state” or the equilibrium between these states is complex to predict and will probably involve such factors as the stability of the conjugate base, the solubility of the formed lithium-conjugate base salt, the coordination of the proton in the electrolyte solution (*e.g.*, H-F hydrogen bonded network) and the consumption of protons by other reactions in the cell – including that ultimately may occur via crossover reactions on anode (in the absence of the glass-ceramic separator). It is challenging to determine the “state” of these species from solution NMR spectra, as the effect of the coordinating ion ( $H^+$  vs  $Li^+$ ) on the chemical shift is not always known and may not have a detectable effect (N.B. the chemical shift difference is noticeable for lithium methoxide and methanol). In the reaction schemes proposed in this work, the  $H^+$ - or  $Li^+$ -equivalent are used as based on the assignments of the chemical shifts and keeping in mind that  $H^+$  ions are generated at the positive electrode, whereas  $OH^-/LiOH$  is generated and  $H^+$  are consumed via reduction to  $H_2$  at the negative electrode. As a result, the proposed reaction schemes may not always be balanced in terms of Li/H; (we have however tried to ensure they are balanced in terms of carbon and O content and formal (carbon) oxidation state).

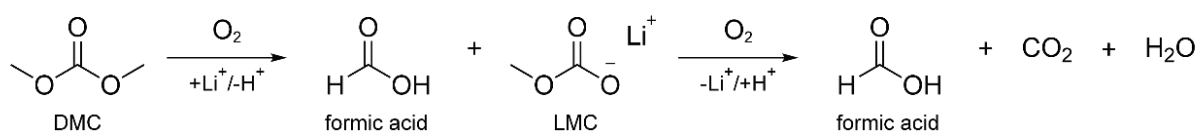
From the  $LiCoO_2/Li$  cell cycled to 4.9 V, *i.e.*, above the gas evolution onset potential, the main decomposition products that were observed on the  $LiCoO_2$  side were formic acid, LMC and glycolic acid/lithium glycolate (Table 2), as well as an increase in the HF/H-bonded proton concentration. The dominant oxidation pathway of the carbonate solvent was determined to proceed via non-Faradaic oxidation. The reactions all involve the addition of oxygen, which strongly supports the proposal that they are associated with or driven by the release of reactive oxygen species at the  $LiCoO_2$  surface; this was the starting point for proposing formation reaction pathways for these decomposition products. Note that the evolution of singlet oxygen ( $^1O_2$ ) from layered transition metal oxides at high electrode potentials has been observed previously by photon emission spectroscopy.<sup>8</sup> Singlet oxygen is an excited state of oxygen that is far more reactive than the triplet ground state ( $^3O_2$ ) and it has been identified as an important cause of degradation in  $Li-O_2$  chemistry<sup>69</sup> and in biological systems.<sup>70</sup> We note, however, that the decomposition reactions may not necessarily involve dissolved  $^1O_2$  but may be coupled with the cathode surface reconstruction process that leads to the oxygen release.

In general, carbon-carbon bonds are very difficult to break (unless extremely reactive radicals are present), because they are strong and not easily polarised. Note that singlet oxygen, while highly reactive, is not a radical but is rather a strong electrophile. Formic acid and LMC do not contain any carbon-carbon bonds, so they are, therefore, presumed to originate from DMC, rather than EC. A possible reaction scheme to form formic acid and LMC via chemical oxidation of DMC is proposed and outlined in (Scheme 2). Firstly, DMC is chemically oxidised with a reactive oxygen species, *e.g.* singlet  $O_2$ , to produce formic acid and LMC. The formation of the semi-carbonate LMC at the positive

electrode may seem surprising, since semi-carbonates are conventionally thought to only form at the negative electrode through the reduction of DMC (Scheme 9b). It is then proposed that LMC could be chemically oxidised again to release more formic acid, as well as CO<sub>2</sub> and water. Alternatively, LMC can react further via hydrolysis, thermal decomposition, reaction with PF<sub>5</sub>, or migrate to the negative electrode where it may be reduced to CO<sub>2</sub><sup>-</sup> and lithium methoxide.<sup>55,71</sup>

*Scheme 2. Proposed reaction scheme for the chemical oxidation of dimethyl carbonate (DMC) to formic acid, CO<sub>2</sub> and water. Lithium methyl carbonate (LMC) (identified here by NMR) is a proposed intermediate.*

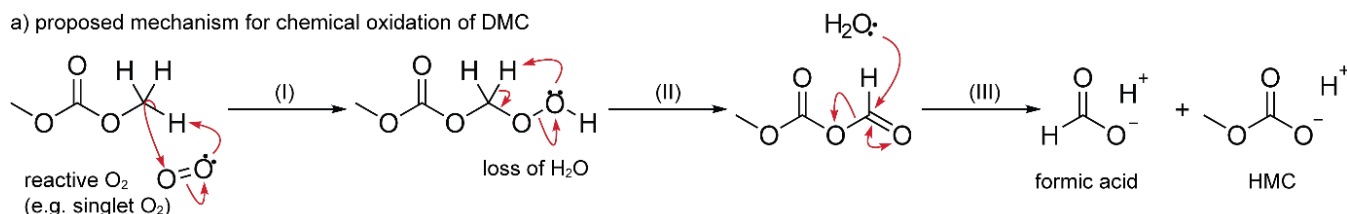
chemical oxidation of DMC



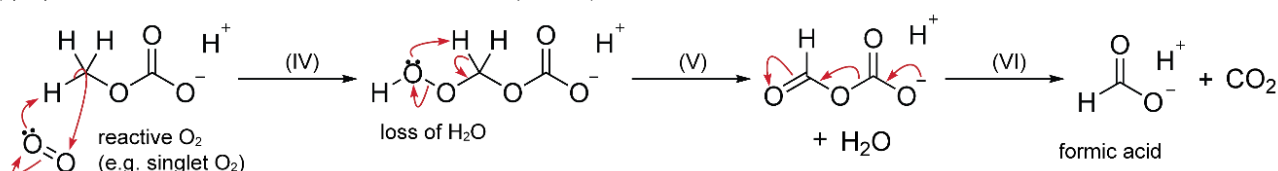
The proposed mechanism for the chemical oxidation of DMC and LMC is given in Scheme 3. A reactive oxygen species deprotonates the methyl group on DMC, followed by nucleophilic attack of the deprotonated carbon onto the second oxygen to form a new carbon-oxygen bond (Scheme 3a, step I). The first oxygen deprotonates the same carbon on DMC again to form an aldehyde unit and release water (step II). The water molecule can attack back into the carbonyl group of the aldehyde to produce formic acid (or lithium formate) and LMC (step III). LMC can be oxidised in a similar way to DMC (Scheme 3b). The main difference is that after forming the aldehyde moiety (step V), the water that is lost does not reattack and the resulting species decomposes to form lithium formate and CO<sub>2</sub>.

*Scheme 3. Proposed mechanism for the chemical oxidation of (a) dimethyl carbonate; DMC and (b) lithium methyl carbonate (LMC).*

a) proposed mechanism for chemical oxidation of DMC



b) proposed mechanism for chemical oxidation of HMC (or LMC)

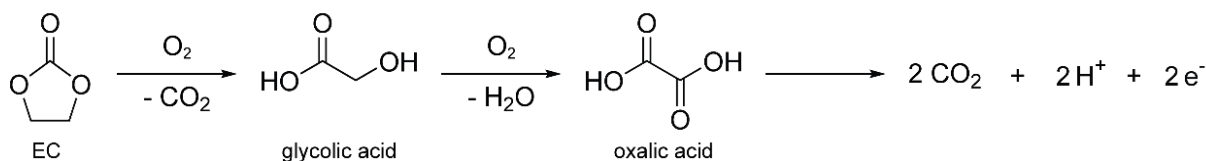


The observed glycolic acid or lithium glycolate is assumed to be a decomposition product of EC and not DMC, on the basis of its two connected carbon atoms; the formation of carbon-carbon bonds at the positive electrode is unlikely, as no reagents or functional groups are present that could facilitate

the formation of such bonds. A possible reaction scheme for the chemical oxidation of EC to glycolic acid and CO<sub>2</sub> is proposed and outlined in Scheme 6. First, EC is chemically oxidised to CO<sub>2</sub> and glycolic acid, which can then be chemically oxidised again to form water and oxalic acid. At this cell potential (4.9 V vs Li/Li<sup>+</sup>), oxalic acid is rapidly oxidised (electrochemically) to CO<sub>2</sub> and H<sup>+</sup>.<sup>72</sup> Thus, the overall reaction equation for the proposed complete chemical oxidation of EC would be  $\text{EC} + 4 \text{O}_{\text{lattice}} \rightarrow 3 \text{CO}_2 + \text{H}_2\text{O} + 2 \text{H}^+$ . Even though the presence of oxalic acid (or lithium oxalate) in the electrolyte could not be determined due to the technique used (<sup>1</sup>H NMR), its low solubility in both the electrolyte and NMR solvent suggests that oxalic acid is more likely found precipitated out on the electrode surface, rather than in the electrolyte. The rapid oxidation of oxalic acid above 4.5 V (vs Li/Li<sup>+</sup>),<sup>72</sup> also suggests that the presence of oxalic acid in the electrolyte is unlikely. The increased proton concentration in the electrolyte provides evidence for the oxidation of oxalic acid but could also be due to the oxidation of water that is formed through carbonate oxidation.

*Scheme 4. Proposed reaction scheme for the chemical oxidation of ethylene carbonate (EC) to 3 CO<sub>2</sub>, H<sub>2</sub>O and 2 H<sup>+</sup>. Glycolic acid and oxalic acid are thought to be intermediates in this reaction. The electrochemical oxidation of oxalic acid is also shown.*

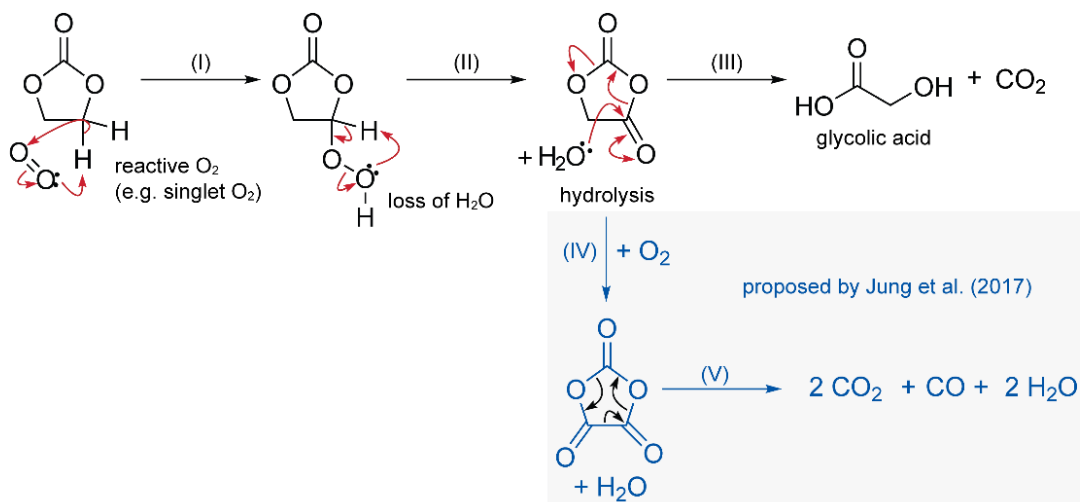
chemical oxidation of EC



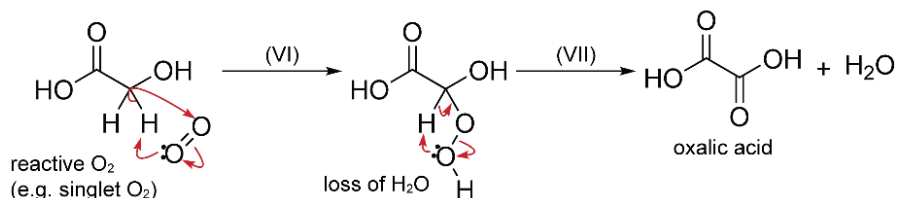
Scheme 5a shows the proposed mechanism for the chemical oxidation of EC and formation of glycolic acid. Steps (I) and (II) are identical to the mechanism proposed for DMC and are not discussed further. The intermediate formed after step (II) can be hydrolysed by the water that is released in the previous step, after which the molecule decarboxylates to form glycolic acid and CO<sub>2</sub> (step III). Nucleophilic attack of water will preferentially occur at the carbonyl group of the ester unit, rather than at the carbonate group, as the ester is more reactive towards nucleophilic attack. Glycolic acid can be chemically oxidised in a similar way to produce oxalic acid and water (Scheme 5b).

Scheme 5. Proposed mechanism for the chemical oxidation of (a) ethylene carbonate (EC) and (b) glycolic acid.

a) proposed mechanism for chemical oxidation of EC



b) proposed mechanism for chemical oxidation of glycolic acid



Gasteiger and co-workers<sup>3</sup> previously proposed that the overall reaction equation for the chemical oxidation of EC at an NMC electrode surface is  $EC + 4 O_{\text{lattice}} \rightarrow 2 CO_2 + CO + 2 H_2O$ , based on OEMS measurements that showed a  $CO_2$  to  $CO$  ratio of 2:1. They suggested a similar mechanism as discussed above (steps I and II), however, they argued that the molecule formed after step II must be oxidised further (step IV), instead of decomposing into formaldehyde,  $CO_2$  and  $CO$ , as no formaldehyde was detected and a higher  $CO_2$  to  $CO$  ratio was observed. However, we suggest that the intermediate formed after step II is highly reactive and could quickly hydrolyse to form glycolic acid, before a second oxidation step occurs. This reaction scheme would also be consistent with the reaction mechanism proposed for the oxidation of DMC. Alternative explanations for the observation of  $CO$  by Jung et al.<sup>3</sup> were therefore considered. Oxidation of water at the conductive carbon would produce  $CO$  and  $2 H^+$ , however, they demonstrated this was not the case using  $^{13}C$ -labelled conductive carbon for OEMS measurements.<sup>22</sup> The  $CO$  production in their NMC/graphite cells was coupled to  $O_2$  release from the transition metal oxide, thus also excluding reduction reactions at the negative electrode. It is therefore proposed that the reaction pathways III and IV in Scheme 5a are competitive with those suggested by Jung et al.,<sup>22</sup> with relative reactions rates that are likely determined by the material- and voltage-dependent kinetics of oxygen loss and mass transport rate of the intermediate. Additional NMR studies using the methods outlined in the present work are suggested to look for glycolic acid or lithium glycolate reaction products at NMC electrodes.

Finally, no evidence for dehydrogenation of EC at the positive electrode to form VC, hydrolysis of EC, nor transesterification of EC or DMC were observed in this work.

#### *CO<sub>2</sub> reduction at the negative electrode*

Chemical oxidation of the carbonate solvent at the positive electrode results in the production of H<sub>2</sub>O and CO<sub>2</sub>. Even though a lithium-ion conducting ceramic is used to inhibit migration of electrolyte decomposition species between the electrodes, CO<sub>2</sub> formed at the positive electrode can pass around the edges of the ceramic and diffuse to the surface of the negative electrode. At the lithium metal surface, CO<sub>2</sub> that is dissolved in the electrolyte, is reduced to a CO<sub>2</sub> radical anion. This radical anion rapidly abstracts a proton from other species in the electrolyte, *e.g.* H<sub>2</sub>O, to form lithium formate, which can be reduced further in a similar way to generate formaldehyde (Scheme 6a). This proposed pathway also produces Li<sub>2</sub>O, a known component in the 'mature' negative electrode SEI.<sup>45</sup>

Other pathways for the reduction of CO<sub>2</sub> that have been reported in the literature include the formation of lithium oxalate (Scheme 6b) and lithium carbonate (Scheme 6c).<sup>72</sup> Neither species contains protons, so they cannot be detected with <sup>1</sup>H NMR, but due to their low solubility in both the electrolyte and the NMR solvent, they are again most likely present on the electrode surface rather than and not in the electrolyte solution. Moreover, Li<sub>2</sub>CO<sub>3</sub> can react with HF formed in the cell via an acid-base reaction to form lithium fluoride (LiF), H<sub>2</sub>O and CO<sub>2</sub>, and may therefore be challenging to detect;<sup>73</sup> it is also known to be removed electrochemically at above 4.2 V.<sup>73,74</sup>

CO<sub>2</sub> can also be produced in cells with lower cut-off voltages via the decomposition of the DMC-reduction product, LMC, or via the decarboxylation of EC-reduction products, *e.g.* lithium alkyl carbonate radicals or polycarbonate oligomers at the negative electrode.<sup>19</sup> However, these reactions are negligible compared to the generation of CO<sub>2</sub> at the positive electrode at high cell voltages,<sup>3,23</sup> and explains why formaldehyde and lithium formation are not observed at lower cell voltages.



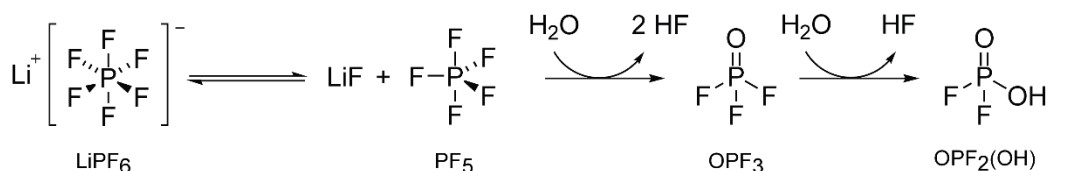
different, which could explain the increased formation of alkoxide/alcohol species in the cell cycled to 4.9 V.

The electrolyte from the lithium metal side also contains silicon fluorides, but only small amounts of  $\text{BF}_4^-$ , whereas the electrolyte from the  $\text{LiCoO}_2$  side has approximately equal quantities of silicon and boron fluorides, both originating from the borosilicate glass fibre separator. The reactivity of silicon oxide is higher than that of boron oxide, hence more silicon fluoride is seen if on the lithium metal side. However, if enough HF is present, as is the case on the  $\text{LiCoO}_2$  side, it can also react with the boron oxide to form  $\text{BF}_4^-$ .

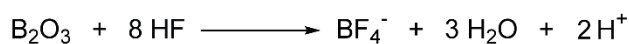
The pristine electrolyte contains  $\text{LiPO}_2\text{F}_2$  (or  $\text{Li}^+\text{OPF}_2(\text{O}^-)$ ) and HF impurities, which form through reaction of the  $\text{LiPF}_6$  salt with trace moisture present in the electrolyte (Scheme 7a top).<sup>51,75</sup>

Scheme 7. (a)  $\text{LiPF}_6$  decomposition pathways,<sup>51,75</sup> and reactions of hydrofluoric acid (HF) with the borosilicate glass fibre separator: (b) reaction between boron oxide ( $\text{B}_2\text{O}_3$ ) and (c) reaction between silicon oxide ( $\text{SiO}_2$ ).

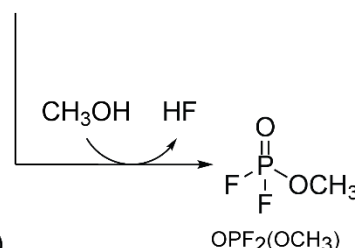
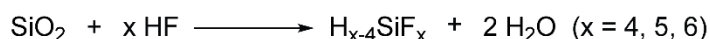
a)  $\text{LiPF}_6$  degradation pathways



b) Reaction of HF with  $\text{B}_2\text{O}_3$



c) Reaction of HF with  $\text{SiO}_2$



The preferential formation of OH-based fluorophosphates at the positive electrode and  $\text{OCH}_3$ -based fluorophosphates at the negative electrode is rationalised by the relative concentrations of water and methanol present at each side. At the negative electrode, the water concentration is presumed to be low, since trace moisture is partially removed at the lithium metal surface by reducing it to  $\text{LiOH}$  and  $\text{H}_2$  gas. Due to DMC reduction at the lithium metal surface, the methanol concentration is most likely higher than that of water, explaining the formation of  $\text{OCH}_3$ -based difluorophosphate species. On the positive electrode side, however, oxidation of the carbonate solvent leads to high water concentrations, therefore the formation of OH-based difluorophosphate species are preferred.

#### *H<sub>2</sub>O at high cell voltages*

Water was not observed in the electrolyte from the  $\text{LiCoO}_2$  half of the cell cycled to 4.9 V, even though it is a proposed product of solvent oxidation. OEMS measurements have shown that water enhances

the anodic oxidation of conductive carbon particles and that this reaction proceeds at 4.8 V vs Li/Li<sup>+</sup>, but can occur at slightly lower potentials if the water concentration is high (4.7 V vs Li/Li<sup>+</sup> for 4000 ppm H<sub>2</sub>O).<sup>22</sup> The water-enhanced corrosion reaction of carbon consumes water and produces CO<sub>2</sub> or CO and protons (Scheme 8a).<sup>22</sup> The resulting protons can form ion pairs with PF<sub>6</sub><sup>-</sup> and decompose the anion to PF<sub>5</sub> and HF (Scheme 8b).<sup>76</sup>

The reactions in Scheme 8a and b are consistent with the appearance of a broad signal in the <sup>1</sup>H NMR spectrum (Figure 3b), which is ascribed to HF and other H-bonded proton species. It has also previously been proposed that protons can intercalate into the partially delithiated transition metal oxide, leading to a loss of active material at the positive electrode (Scheme 8c).<sup>48</sup>

The absence of water in the electrolyte is not attributed to the consumption of water via hydrolysis of the LiPF<sub>6</sub> salt or the carbonate solvent. Increased LiPF<sub>6</sub> decomposition due to the reaction with water is observed, however, this reaction is relatively slow, supported by the presence of some water in other electrolytes in this work. Furthermore, only trace quantities of methanol (a hydrolysis product of DMC) and no observable amounts of LEMC or EG (hydrolysis products of EC) are observed. Therefore, hydrolysis of the salt and the solvent only represent minor processes for the consumption of water.

*Scheme 8. Reaction schemes for (a) the water-enhanced anodic oxidation of carbon,<sup>22</sup> (b) the acid-catalysed decomposition of PF<sub>6</sub><sup>-</sup><sup>76</sup> and (c) the intercalation of H<sup>+</sup> into the (partially) delithiated transition metal oxide.<sup>48</sup>*

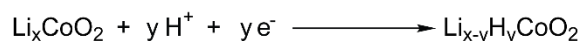
a) water-enhanced anodic oxidation of carbon



b) acid-catalysed decomposition of PF<sub>6</sub><sup>-</sup>



c) intercalation of H<sup>+</sup> into delithiated LiCoO<sub>2</sub>



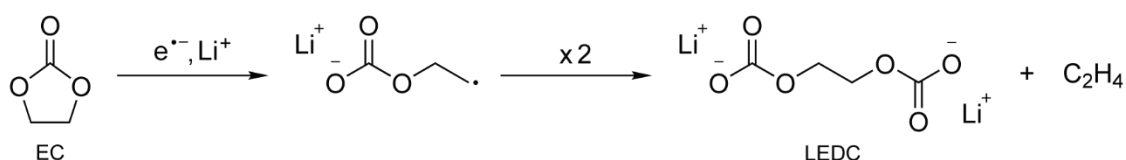
### *Reduction of the carbonate solvent at the negative electrode*

The reduction products and pathways of EC and DMC have previously been studied extensively and reviewed.<sup>45,77</sup> The electrolyte decomposition products observed at the lithium metal side of the LiCoO<sub>2</sub>/Li cells in the present work include LEDC and LEMC, consistent with previous literature. Both are proposed to originate from EC, and the remaining observed products, LMC, lithium methoxide, lithium succinate and methanol were also observed to originate from the DMC.<sup>27,78</sup> Scheme 9a shows the reduction of EC to LEDC; EC is reduced via a one-electron ring-opening reaction, forming a lithium

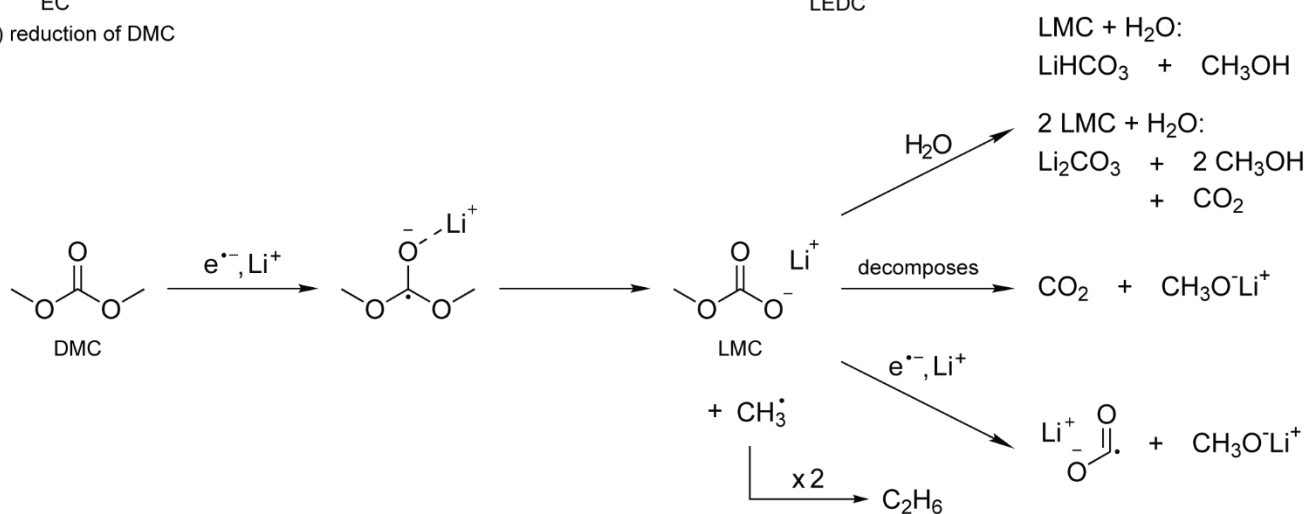
alkyl carbonate radical, which dimerises to form LEDC and release ethene gas.<sup>55,78,79</sup> The reduction of DMC (Scheme 9b) also proceeds via a one-electron reaction forming a lithium alkyl carbonate radical that decomposes into lithium methyl carbonate (LMC) and a  $\text{CH}_3^\bullet$  radical.<sup>27,78</sup> This  $\text{CH}_3^\bullet$  radical dimerises to form ethane gas. LMC can react further in several ways: it can decompose to release  $\text{CO}_2$  gas and to form lithium methoxide, it can react with water to form a mixture of carbonates, methanol and  $\text{CO}_2$ , or it can be reduced further to generate lithium methoxide and a  $\text{CO}_2^\bullet$  radical.<sup>27,78</sup> This radical, can also be formed through the reduction of  $\text{CO}_2$  and results in the formation of various products, one of which is lithium succinate (Scheme 9c).<sup>80</sup> This mechanism is proposed based on previous literature and is consistent with the signatures of lithium succinate in the  $^1\text{H}$  NMR spectra (Figure 3a and b).

*Scheme 9. Summary of reduction reactions at the negative electrode consistent with the chemical signatures detected by solution NMR. a) The reduction of ethylene carbonate (EC) to lithium ethylene dicarbonate (LEDC).<sup>55,78,79</sup> b) The reduction of dimethyl carbonate (DMC) to lithium methyl carbonate (LMC) and further reactions of LMC.<sup>27,78</sup> c) The formation of lithium succinate.<sup>80</sup>*

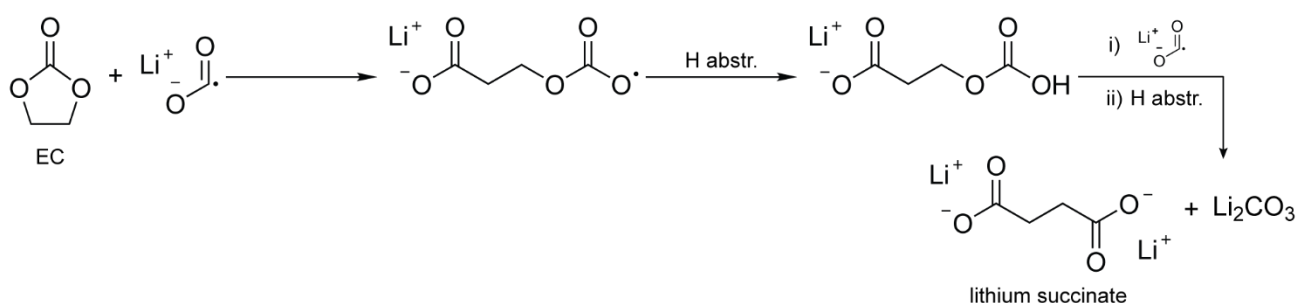
a) reduction of EC to lithium ethylene dicarbonate (LEDC)



b) reduction of DMC



c) formation of lithium succinate

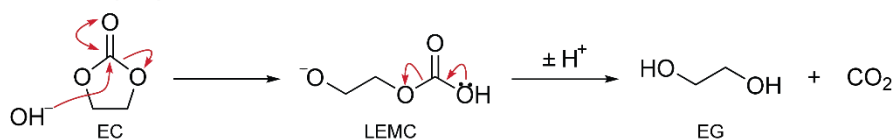


Not all electrolyte decomposition reactions are electrochemical in nature or even involve a reduction or oxidation step; some decomposition proceeds via non-redox reactions. For example, LEMC can

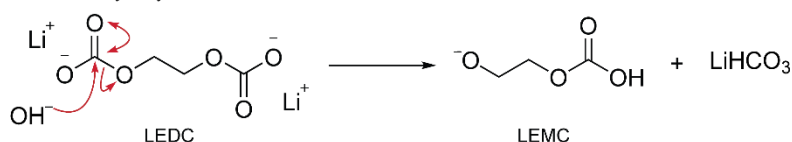
form either through the hydrolysis of EC (purely chemical; Scheme 10a) or from the hydrolysis of LEDC (Scheme 10b). Even though the H<sub>2</sub>O-driven hydrolysis of EC does not proceed at appreciable rates at room temperature, the OH<sup>-</sup> driven (*i.e.*, base-catalysed) hydrolysis of EC is appreciable at room temperature, as OH<sup>-</sup> is a stronger nucleophile.<sup>47</sup> Sources of OH<sup>-</sup> in the electrolyte include the reduction of trace moisture at the negative electrode to form LiOH or OH<sup>-</sup> and H<sub>2</sub> gas, the reduced anode representing a highly basic environment (noting of course the difficulty in defining basicity in non-aqueous solvents). LEMC could decompose further to ethylene glycol (EG) and CO<sub>2</sub>, but no evidence for EG ( $\delta$  <sup>1</sup>H = 3.40 ppm; s)<sup>52</sup> is observed in our <sup>1</sup>H NMR spectra. The formation of LMC, lithium methoxide and methanol could similarly be explained via the hydrolysis of DMC (Scheme 10c), in addition to the electrochemically-induced pathways described in Scheme 9b. Evidence that these species can form through hydrolysis is provided by the <sup>1</sup>H NMR spectrum of electrolyte deliberately spiked with 100,000 ppm water after storage for 2 months (Figure S 21), which shows the presence of LEMC, LMC, lithium methoxide and methanol (see SI for more details).

*Scheme 10. The base-driven hydrolysis reactions of (a) ethylene carbonate (EC) to lithium ethylene monocarbonate (LEMC), which can decompose to ethylene glycol (EG) and CO<sub>2</sub>, (b) lithium ethylene dicarbonate (LEDC) to LEMC and lithium hydrogen carbonate, and (c) dimethyl carbonate (DMC) to lithium methyl carbonate (LMC) and methoxide.*

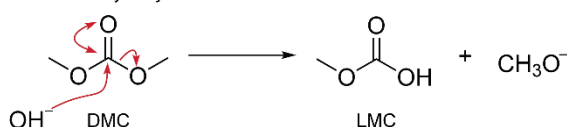
a) base-driven hydrolysis of EC



b) base-driven hydrolysis of LEDC



c) base-driven hydrolysis of DMC



### Summary of electrolyte decomposition at high voltages

An overview of the electrolyte decomposition reactions that occur at high voltages (high SOC) was given in Figure 6, and can now be discussed in the context of the various mechanistic schemes proposed above. Reactive oxygen species released from the transition metal oxide particles chemically oxidise the carbonate solvent, producing carboxylic acids and semi-carbonates and releasing CO<sub>2</sub> and water (Scheme 2 and Scheme 4). The CO<sub>2</sub> that is produced migrates to the negative electrode, where it is first reduced to lithium formate and then formaldehyde, but other reduction

products (lithium carbonate, lithium oxalate) could be formed too (Scheme 6). The water that is formed hydrolyses the  $\text{LiPF}_6$  salt, producing fluorophosphate species and HF, which in turn can attack various components of the cell (*e.g.* separator, active material at positive electrode; Scheme 7). Water also enhances the anodic oxidation of the conductive carbon particles, raising the concentration of protic species in the electrolyte (Scheme 8). An overview of the electrolyte decomposition reactions that occur including those at the negative electrode is given in Figure S 22.

The scheme of electrolyte decomposition reactions in a cell without a lithium-ion conducting ceramic will be inherently more complex as it will involve electrode cross-talk (*i.e.*, the migration of species formed at one electrode to the other electrode, where they may react further). This process, well-known for gases, may lead to the consumption of the species in Figure 6 (or Figure S 22) or the generation of additional species, other than those identified in this work.

#### *Implications of decomposition products and mechanisms*

It is noted that oxygen loss is less documented in  $\text{LiCoO}_2$  than in higher nickel content materials, especially the NMCs, in part because  $\text{LiCoO}_2$  is not generally operated at such high potentials. The chemical oxidation of electrolyte at the positive electrode, especially at higher states of charge, directly leads to increased gas evolution in the cell and impedance growth at the positive electrode, due to the deposition of decomposition species on the surface. This process is expected to proceed independently of the negative electrode chemistry (*i.e.*, Li, graphite,  $\text{Li}_4\text{Ti}_5\text{O}_{12}$ , etc.). The production of dissolved protons (water oxidation) and HF ( $\text{LiPF}_6$  hydrolysis), can lead to intercalation of  $\text{H}^+$  into the positive electrode and lead to enhanced transition metal dissolution rates from the active material; both processes will lead to a loss of the available active material, in addition to the O loss that causes this in the first place. The dissolved transition metals ions can then migrate to the anode surface and reductively deposit, where they can disrupt the SEI and catalyse electrolyte reduction, leading to irreversible loss of active  $\text{Li}^+$ -ions and impedance growth.<sup>15</sup> Electrolyte oxidation products formed at the cathode can also migrate to the anode, where they will be reduced and deposited on the surface, further increasing the cell impedance.<sup>16,17</sup> Over several charge-discharge cycles, this layer will build up and can limit ion transport to the bulk of the anode (interfacial kinetic hinderance), which can make significant contribution to the capacity fade (especially at high rates).<sup>81,82</sup> The loss of active material and the various reactions of the decomposition products at both electrodes can also cause cell slippage (*i.e.*, a mismatch of the relative capacity-voltage curves for each electrode) and a further decrease in the available capacity.

Decomposition of the electrolyte will not only affect the electrodes, but also the physical chemical properties of the electrolyte itself. For example, decomposition of the  $\text{LiPF}_6$  will lead to a decrease in

the lithium salt concentration in the electrolyte. If an asymmetrical alkyl carbonate solvent such as ethyl methyl carbonate, EMC, is used, then trans-esterification can affect the relative concentrations of the solvent components. Both of these changes can have significant effects on the solution properties, such as melting point, conductivity, and viscosity. These changes may have importance for cell performance in low-temperature and high-rate applications.

Future studies will examine chemical reactivity with singlet oxygen generated directly and the role that catalysis of these reactions by the transition metal oxide surfaces, or coupled metal-ion reduction, oxygen loss, and electrolyte degradation mechanisms<sup>40-44</sup> - proposed to be important in Ni-containing systems – play in controlling the potentials of both electrolyte degradation and oxygen loss.

## Conclusions

This work has utilised specially designed LiCoO<sub>2</sub>/Li cells in which the anode and cathode compartments were separated by a lithium-ion conducting glass-ceramic to examine electrolyte degradation of a standard lithium-ion battery electrolyte. The benefit of this approach is that electrolyte decomposition products formed under different cycling conditions could be independently identified at each electrode, without the complication of “cross-talk” or shuttling effects. The oxidation products resulting from electrochemical oxidation of electrolyte solution was studied in an H-cell. Of note, significant electro-osmotic flow was detected in the H-cell experiments, and the role that this has on battery performance particularly at high rates merits further investigation.

The analysis of the decomposition products detected by NMR spectroscopy was used to construct a detailed reaction scheme which accounts for all the observed decomposition products and attempts to rationalise the formation of products proposed in prior studies that were detected via complementary analytical techniques (Figure 6). One principal finding is that chemical oxidation driven by oxygen loss, rather than electrochemical oxidation, is the dominant driver for electrolyte decomposition at the positive electrode surface at high voltages. It is emphasised that the oxidative decomposition of the electrolyte at the positive electrode is intrinsically linked to surface reactivity of the active material. It is therefore suggested that an understanding the electrode-electrolyte interfacial chemistry will benefit research into improving cell lifetime at higher upper cut-off voltages. It is hoped that the present work will assist future studies to consider the underlying chemical mechanisms and kinetics for controlling oxygen loss when, for example, designing surface coatings, doping of the cathodes to increase stability, and electrolyte additives.

**Acknowledgements**

This work was supported by US Department of Energy [DE-SC0012583 (68799)], the Faraday Institution [FIRG001], Engineering and Physical Sciences Research Council [EP/M009521/1 (DJR00640)], and the European Research Council [EC H2020 ERC (835073)].

## References

- (1) Quinn, J. B.; Waldmann, T.; Richter, K.; Kasper, M.; Wohlfahrt-Mehrens, M. Energy Density of Cylindrical Li-Ion Cells: A Comparison of Commercial 18650 to the 21700 Cells. *J. Electrochem. Soc.* **2018**, *165* (14), A3284–A3291. <https://doi.org/10.1149/2.0281814jes>.
- (2) Glazier, S. L.; Nelson, K. J.; Allen, J. P.; Li, J.; Dahn, J. R. The Effect of Different Li(Ni<sub>1-x-y</sub>Mn<sub>x</sub>Co<sub>y</sub>)O<sub>2</sub> Positive Electrode Materials and Coatings on Parasitic Heat Flow as Measured by Isothermal Microcalorimetry, Ultra-High Precision Coulometry and Long Term Cycling. *J. Electrochem. Soc.* **2017**, *164* (6), A1203–A1212. <https://doi.org/10.1149/2.1121706jes>.
- (3) Jung, R.; Metzger, M.; Maglia, F.; Stinner, C.; Gasteiger, H. A. Oxygen Release and Its Effect on the Cycling Stability of LiNi<sub>x</sub>Mn<sub>y</sub>Co<sub>z</sub>O<sub>2</sub> (NMC) Cathode Materials for Li-Ion Batteries. *J. Electrochem. Soc.* **2017**, *164* (7), A1361–A1377. <https://doi.org/10.1149/2.0021707jes>.
- (4) Nelson, K. J.; Harlow, J. E.; Dahn, J. R. A Comparison of NMC/Graphite Pouch Cells and Commercially Available LiCoO<sub>2</sub>/Graphite Pouch Cells Tested to High Potential. *J. Electrochem. Soc.* **2018**, *165* (3), A456–A462. <https://doi.org/10.1149/2.0041803jes>.
- (5) Lin, F.; Markus, I. M.; Nordlund, D.; Weng, T. C.; Asta, M. D.; Xin, H. L.; Doeff, M. M. Surface Reconstruction and Chemical Evolution of Stoichiometric Layered Cathode Materials for Lithium-Ion Batteries. *Nat. Commun.* **2014**, *5*, 3529. <https://doi.org/10.1038/ncomms4529>.
- (6) Strehle, B.; Kleiner, K.; Jung, R.; Chesneau, F.; Mendez, M.; Gasteiger, H. A.; Piana, M. The Role of Oxygen Release from Li- and Mn-Rich Layered Oxides during the First Cycles Investigated by On-Line Electrochemical Mass Spectrometry. *J. Electrochem. Soc.* **2017**, *164* (2), A400–A406. <https://doi.org/10.1149/2.1001702jes>.
- (7) Zheng, H.; Sun, Q.; Liu, G.; Song, X.; Battaglia, V. S. Correlation between Dissolution Behavior and Electrochemical Cycling Performance for LiNi<sub>1/3</sub>Co<sub>1/3</sub>Mn<sub>1/3</sub>O<sub>2</sub>-Based Cells. *J. Power Sources* **2012**, *207*, 134–140. <https://doi.org/10.1016/j.jpowsour.2012.01.122>.
- (8) Wandt, J.; Freiberg, A. T. S.; Ogrodnik, A.; Gasteiger, H. A. Singlet Oxygen Evolution from Layered Transition Metal Oxide Cathode Materials and Its Implications for Lithium-Ion Batteries. *Mater. Today* **2018**, *21* (8), 825–833. <https://doi.org/10.1016/j.mattod.2018.03.037>.
- (9) Wang, K.; Wan, J.; Xiang, Y.; Zhu, J.; Leng, Q.; Wang, M.; Xu, L.; Yang, Y. Recent Advances and Historical Developments of High Voltage Lithium Cobalt Oxide Materials for Rechargeable Li-Ion Batteries. *J. Power Sources* **2020**, *460* (April), 228062. <https://doi.org/10.1016/j.jpowsour.2020.228062>.
- (10) Li, M.; Lu, J.; Chen, Z.; Amine, K. 30 Years of Lithium-Ion Batteries. **2018**, *1800561*, 1–24. <https://doi.org/10.1002/adma.201800561>.
- (11) Kalluri, S.; Yoon, M.; Jo, M.; Park, S.; Myeong, S.; Kim, J. Surface Engineering Strategies of Layered LiCoO<sub>2</sub> Cathode Material to Realize High-Energy and High-Voltage Li-Ion Cells. **2020**. <https://doi.org/10.1002/aenm.201601507>.
- (12) Zhou, A.; Liu, Q.; Wang, Y.; Wang, W.; Yao, X.; Hu, W.; Zhang, L.; Yu, X.; Li, J.; Li, H. Al<sub>2</sub>O<sub>3</sub> Surface Coating on LiCoO<sub>2</sub> through a Facile and Scalable Wet-Chemical Method towards High-Energy Cathode Materials Withstanding High Cutoff Voltages. **2017**, 24361–24370. <https://doi.org/10.1039/c7ta07312g>.
- (13) Thompson, L. M.; Stone, W.; Eldesoky, A.; Smith, N. K.; McFarlane, C. R. M.; Kim, J. S.; Johnson, M. B.; Petibon, R.; Dahn, J. R. Quantifying Changes to the Electrolyte and Negative Electrode in Aged NMC532 / Graphite Lithium-Ion Cells. *J. Electrochem. Soc.* **2018**, *165* (11), 2732–2740. <https://doi.org/10.1149/2.0721811jes>.
- (14) Ma, X.; Harlow, J. E.; Li, J.; Ma, L.; Hall, D. S.; Genovese, M.; Cormier, M.; Dahn, J. R.; Buteau, S. Hindering Rollover Failure of Li[Ni<sub>0.5</sub>Mn<sub>0.3</sub>Co<sub>0.2</sub>]O<sub>2</sub>/Graphite Pouch Cells during Long-Term Cycling. *J. Electrochem. Soc.* **2019**, *166* (4), A711–A724. <https://doi.org/10.1149/2.0801904jes>.
- (15) Wandt, J.; Freiberg, A.; Thomas, R.; Gorlin, Y.; Siebel, A.; Jung, R.; Gasteiger, H. A.; Tromp, M.

- Transition Metal Dissolution and Deposition in Li-Ion Batteries Investigated by Operando X-Ray Absorption Spectroscopy. *J. Mater. Chem. A* **2016**, *4* (47), 18300–18305. <https://doi.org/10.1039/C6TA08865A>.
- (16) Dedryvère, R.; Foix, D.; Franger, S.; Patoux, S.; Daniel, L.; Gonbeau, D. Electrode/Electrolyte Interface Reactivity in High-Voltage Spinel LiMn<sub>1.6</sub>Ni<sub>0.4</sub>O<sub>4</sub>/Li<sub>4</sub>Ti<sub>5</sub>O<sub>12</sub> Lithium-Ion Battery. *J. Phys. Chem. C* **2010**, *114* (24), 10999–11008. <https://doi.org/10.1021/jp1026509>.
- (17) Xiong, D. J.; Ellis, L. D.; Nelson, K. J.; Hynes, T.; Petibon, R.; Dahn, J. R. Rapid Impedance Growth and Gas Production at the Li-Ion Cell Positive Electrode in the Absence of a Negative Electrode. **2016**, *163* (14). <https://doi.org/10.1149/2.1031614jes>.
- (18) Harris, Oliver, C.; Lee, Sophia, E.; Lees, C.; Tang, M. Review: Mechanisms and Consequences of Chemical Cross-Talk in Advanced Li-Ion Batteries. *J. Phys. Energ* **2020**.
- (19) Metzger, M.; Strehle, B.; Solchenbach, S.; Gasteiger, H. A. Origin of H<sub>2</sub> Evolution in LIBs: H<sub>2</sub>O Reduction vs. Electrolyte Oxidation. *J. Electrochem. Soc.* **2016**, *163* (5), A798–A809. <https://doi.org/10.1149/2.1151605jes>.
- (20) Imhof, R. Oxidative Electrolyte Solvent Degradation in Lithium-Ion Batteries: An In Situ Differential Electrochemical Mass Spectrometry Investigation. *J. Electrochem. Soc.* **1999**, *146* (5), 1702. <https://doi.org/10.1149/1.1391829>.
- (21) Jung, R.; Metzger, M.; Maglia, F.; Stinner, C.; Gasteiger, H. A. Chemical versus Electrochemical Electrolyte Oxidation on NMC111, NMC622, NMC811, LNMO, and Conductive Carbon. *J. Phys. Chem. Lett.* **2017**, *8* (19), 4820–4825. <https://doi.org/10.1021/acs.jpcclett.7b01927>.
- (22) Metzger, M.; Marino, C.; Sicklinger, J.; Haering, D.; Gasteiger, H. A. Anodic Oxidation of Conductive Carbon and Ethylene Carbonate in High-Voltage Li-Ion Batteries Quantified by On-Line Electrochemical Mass Spectrometry. *J. Electrochem. Soc.* **2015**, *162* (7), A1123–A1134. <https://doi.org/10.1149/2.0951506jes>.
- (23) Freiberg, A. T. S.; Roos, M. K.; Wandt, J.; De Vivie-Riedle, R.; Gasteiger, H. A. Singlet Oxygen Reactivity with Carbonate Solvents Used for Li-Ion Battery Electrolytes. *J. Phys. Chem. A* **2018**, *122* (45), 8828–8839. <https://doi.org/10.1021/acs.jpca.8b08079>.
- (24) Solchenbach, S.; Metzger, M.; Egawa, M.; Beyer, H.; Gasteiger, H. A. Quantification of PF 5 and POF 3 from Side Reactions of LiPF 6 in Li-Ion Batteries. *J. Electrochem. Soc.* **2018**, *165* (13), A3022–A3028. <https://doi.org/10.1149/2.0481813jes>.
- (25) Petibon, R.; Rotermund, L.; Nelson, K. J.; Gozdz, A. S.; Xia, J.; Dahn, J. R. Study of Electrolyte Components in Li Ion Cells Using Liquid-Liquid Extraction and Gas Chromatography Coupled with Mass Spectrometry. *J. Electrochem. Soc.* **2014**, *161* (6), A1167–A1172. <https://doi.org/10.1149/2.117406jes>.
- (26) Laszczynski, N.; Solchenbach, S.; Gasteiger, H. A.; Lucht, B. L. Understanding Electrolyte Decomposition of Graphite/NCM811 Cells at Elevated Operating Voltage. *J. Electrochem. Soc.* **2019**, *166* (10), A1853–A1859. <https://doi.org/10.1149/2.0571910jes>.
- (27) Dedryvère, R.; Bonhomme, F.; Biensan, P.; Gonbeau, D. Surface Film Formation on Electrodes in a LiCoO<sub>2</sub> / Graphite Cell : A Step by Step XPS Study. **2007**, *174*, 462–468. <https://doi.org/10.1016/j.jpowsour.2007.06.033>.
- (28) Madec, L.; Ellis, L. D. Exploring Interactions between Electrodes in Li[Ni<sub>x</sub>Mn<sub>y</sub>Co<sub>1-x-y</sub>]O<sub>2</sub> /Graphite Cells through Electrode/Electrolyte Interfaces Analysis. *J. Electrochem. Soc.* **2017**, *164* (14), A3718–A3726. <https://doi.org/10.1149/2.1011714jes>.
- (29) Louli, A. J.; Ellis, L. D.; Dahn, J. R. Operando Pressure Measurements Reveal Solid Electrolyte Interphase Growth to Rank Li-Ion Cell Performance. *Joule* **2019**, *3* (3), 745–761. <https://doi.org/10.1016/j.joule.2018.12.009>.
- (30) Madec, L.; Xia, J.; Petibon, R.; Nelson, K. J.; Sun, J. P.; Hill, I. G.; Dahn, J. R. Effect of Sulfate Electrolyte Additives on LiNi<sub>1/3</sub>Mn<sub>1/3</sub>Co<sub>1/3</sub>O<sub>2</sub>/Graphite Pouch Cell Lifetime: Correlation between Xps Surface Studies and Electrochemical Test Results. *J. Phys. Chem. C* **2014**, *118* (51), 29608–29622. <https://doi.org/10.1021/jp509731y>.

- (31) Glazier, S. L.; Odom, S. A.; Kaur, A. P.; Dahn, J. R. Determining Parasitic Reaction Enthalpies in Lithium-Ion Cells Using Isothermal Microcalorimetry. *J. Electrochem. Soc.* **2018**, *165* (14), A3449–A3458. <https://doi.org/10.1149/2.0761814jes>.
- (32) Logan, E. R.; Hebecker, H.; Ma, X.; Quinn, J.; HyeJeong, Y.; Kumakura, S.; Paulsen, J.; Dahn, J. R. A Comparison of the Performance of Different Morphologies of LiNi<sub>0.8</sub>Mn<sub>0.1</sub>Co<sub>0.1</sub>O<sub>2</sub> Using Isothermal Microcalorimetry, Ultra-High Precision Coulometry, and Long-Term Cycling. *J. Electrochem. Soc.* **2020**, *167* (6), 060530. <https://doi.org/10.1149/1945-7111/ab8620>.
- (33) Day, R. P.; Xia, J.; Petibon, R.; Rucska, J.; Wang, H.; Wright, A. T. B.; Dahn, J. R. Differential Thermal Analysis of Li-Ion Cells as an Effective Probe of Liquid Electrolyte Evolution during Aging. *J. Electrochem. Soc.* **2015**, *162* (14), A2577–A2581. <https://doi.org/10.1149/2.0181514jes>.
- (34) Xing, L.; Li, W.; Wang, C.; Gu, F.; Xu, M.; Tan, C.; Yi, J. Theoretical Investigations on Oxidative Stability of Solvents and Oxidative Decomposition Mechanism of Ethylene Carbonate for Lithium Ion Battery Use. *J. Phys. Chem. B* **2009**, *113* (52), 16596–16602. <https://doi.org/10.1021/jp9074064>.
- (35) Zhang, X.; Pugh, J. K.; Ross, P. N. Computation of Thermodynamic Oxidation Potentials of Organic Solvents Using Density Functional Theory. *J. Electrochem. Soc.* **2001**, *148* (5), E183. <https://doi.org/10.1149/1.1362546>.
- (36) Tebbe, J. L.; Fuerst, T. F.; Musgrave, C. B. Degradation of Ethylene Carbonate Electrolytes of Lithium Ion Batteries via Ring Opening Activated by LiCoO<sub>2</sub> Cathode Surfaces and Electrolyte Species. *ACS Appl. Mater. Interfaces* **2016**, *8* (40), 26664–26674. <https://doi.org/10.1021/acsami.6b06157>.
- (37) Xu, K. Toward Reliable Values of Electrochemical Stability Limits for Electrolytes. *J. Electrochem. Soc.* **1999**, *146* (11), 4172. <https://doi.org/10.1149/1.1392609>.
- (38) Abe, K.; Ushigoe, Y.; Yoshitake, H.; Yoshio, M. Functional Electrolytes: Novel Type Additives for Cathode Materials, Providing High Cycleability Performance. *J. Power Sources* **2006**, *153* (2), 328–335. <https://doi.org/10.1016/j.jpowsour.2005.05.067>.
- (39) Moshkovich, M.; Cojocar, M.; Gottlieb, H. E.; Aurbach, D. The Study of the Anodic Stability of Alkyl Carbonate Solutions by in Situ FTIR Spectroscopy, EQCM, NMR and MS. *J. Electroanal. Chem.* **2001**, *497*, 84–96. [https://doi.org/http://dx.doi.org/10.1016/S0022-0728\(00\)00457-5](https://doi.org/http://dx.doi.org/10.1016/S0022-0728(00)00457-5).
- (40) Jiang, M.; Key, B.; Meng, Y. S.; Grey, C. P. Electrochemical and Structural Study of the Layered, “Li-Excess” Lithium-Ion Battery Electrode Material Li[Li<sub>1/9</sub>Ni<sub>1/3</sub>Mn<sub>5/9</sub>]O<sub>2</sub>. *Chem. Mater.* **2009**, *21* (13), 2733–2745. <https://doi.org/10.1021/cm900279u>.
- (41) Self, J.; Hall, D. S.; Madec, L.; Dahn, J. R. The Role of Prop-1-Ene-1,3-Sultone as an Additive in Lithium-Ion Cells. *J. Power Sources* **2015**, *298*, 369–378. <https://doi.org/10.1016/j.jpowsour.2015.08.060>.
- (42) Muto, S.; Soc, J. E.; Muto, S.; Sasano, Y.; Tatsumi, K.; Sasaki, T. Capacity-Fading Mechanisms of LiNiO<sub>2</sub>-Based Lithium-Ion Batteries : II . Diagnostic Analysis by Electron Microscopy and Spectroscopy. *J. Electrochem. Soc.* **2009**, *156* (5), A371–A377. <https://doi.org/10.1149/1.3076137>.
- (43) Zheng, S.; Huang, R.; Makimura, Y.; Ukyo, Y. Microstructural Changes in LiNi<sub>0.8</sub>Co<sub>0.15</sub>Al<sub>0.05</sub>O<sub>2</sub> Positive Electrode Material during the First Cycle. *J. Electrochem. Soc.* **2011**, *158* (4), A357–A362. <https://doi.org/10.1149/1.3544843>.
- (44) Makimura, Y.; Soc, J. E.; Makimura, Y.; Zheng, S.; Ikuhara, Y.; Ukyo, Y. Microstructural Observation of LiNi<sub>0.8</sub>Co<sub>0.15</sub>Al<sub>0.05</sub>O<sub>2</sub> after Charge and Discharge by Scanning Transmission Electron Microscopy. *J. Electrochem. Soc.* **2012**, *159* (7), A1070–A1073. <https://doi.org/10.1149/2.073207jes>.
- (45) Heiskanen, S. K.; Kim, J.; Lucht, B. L. Generation and Evolution of the Solid Electrolyte Interphase of Lithium-Ion Batteries. *Joule* **2019**, *3* (10), 2322–2333. <https://doi.org/10.1016/j.joule.2019.08.018>.
- (46) Metzger, M.; Strehle, B.; Solchenbach, S.; Gasteiger, H. A. Hydrolysis of Ethylene Carbonate

- with Water and Hydroxide under Battery Operating Conditions. *J. Electrochem. Soc.* **2016**, *163* (7), A1219–A1225. <https://doi.org/10.1149/2.0411607jes>.
- (47) Self, J.; Aiken, C. P.; Petibon, R.; Dahn, J. R. Survey of Gas Expansion in Li-Ion NMC Pouch Cells. *J. Electrochem. Soc.* **2015**, *162* (6), A796–A802. <https://doi.org/10.1149/2.0081506jes>.
- (48) Amatucci, G. G.; Tarascon, J.-M.; Klein, L. C. CoO<sub>2</sub>, The End Member of the LiCoO<sub>2</sub> Solid Solution. *J. Electrochem. Soc.* **1996**, *143* (3), 1114–1123.
- (49) Chen, Z.; Dahn, J. R. Methods to Obtain Excellent Capacity Retention in LiCoO<sub>2</sub> Cycled to 4.5 V. *Electrochim. Acta* **2004**, *49* (7), 1079–1090. <https://doi.org/10.1016/j.electacta.2003.10.019>.
- (50) Ravdel, B.; Abraham, K. M.; Gitzendanner, R.; DiCarlo, J.; Lucht, B.; Campion, C. Thermal Stability of Lithium-Ion Battery Electrolytes. *J. Power Sources* **2003**, *119–121*, 805–810. [https://doi.org/10.1016/S0378-7753\(03\)00257-X](https://doi.org/10.1016/S0378-7753(03)00257-X).
- (51) Campion, C. L.; Li, W.; Lucht, B. L. Thermal Decomposition of LiPF<sub>6</sub>-Based Electrolytes for Lithium-Ion Batteries. *J. Electrochem. Soc.* **2005**, *152* (12), A2327–A2334. <https://doi.org/10.1149/1.2083267>.
- (52) Fulmer, G. R.; Miller, A. J. M.; Sherden, N. H.; Gottlieb, H. E.; Nudelman, A.; Stoltz, B. M.; Bercaw, J. E.; Goldberg, K. I. NMR Chemical Shifts of Trace Impurities: Common Laboratory Solvents, Organics, and Gases in Deuterated Solvents Relevant to the Organometallic Chemist. *Organometallics* **2010**, *29* (9), 2176–2179. <https://doi.org/10.1021/om100106e>.
- (53) Shenderovich, I. G.; Smirnov, S. N.; Denisov, G. S.; Gindin, V. A.; Golubev, N. S.; Dunger, A.; Reibke, R.; Kirpekar, S.; Malkina, O. L.; Limbach, H. H. Nuclear Magnetic Resonance of Hydrogen Bonded Clusters B between F- and (HF)<sub>n</sub>: Experiment and Theory. *Berichte der Bunsengesellschaft/Physical Chem. Chem. Phys.* **1998**, *102* (3), 422–428. <https://doi.org/10.1002/bbpc.19981020322>.
- (54) Shenderovich, I. G.; Tolstoy, P. M.; Golubev, N. S.; Smirnov, S. N.; Denisov, G. S.; Limbach, H. H. Low-Temperature NMR Studies of the Structure and Dynamics of a Novel Series of Acid-Base Complexes of HF with Collidine Exhibiting Scalar Couplings across Hydrogen Bonds. *J. Am. Chem. Soc.* **2003**, *125* (38), 11710–11720. <https://doi.org/10.1021/ja029183a>.
- (55) Xu, K.; Zhuang, G. V.; Allen, J. L.; Lee, U.; Zhang, S. S.; Ross, P. N.; Jow, T. R. Syntheses and Characterization of Lithium Alkyl Mono- and Bicarbonates as Components of Surface Films in Li-Ion Batteries. *J. Phys. Chem. B* **2006**, *110* (15), 7708–7719. <https://doi.org/10.1021/jp0601522>.
- (56) Zhuang, G. V.; Xu, K.; Yang, H.; Jow, T. R.; Ross, P. N. Lithium Ethylene Dicarboxylate Identified as the Primary Product of Chemical and Electrochemical Reduction of EC in 1.2 M LiPF<sub>6</sub>/EC:EMC Electrolyte. *J. Phys. Chem. B* **2005**, *109* (37), 17567–17573. <https://doi.org/10.1021/jp052474w>.
- (57) Babij, N. R.; McCusker, E. O.; Whiteker, G. T.; Canturk, B.; Choy, N.; Creemer, L. C.; Amicis, C. V. D.; Hewlett, N. M.; Johnson, P. L.; Knobelsdorf, J. A.; et al. NMR Chemical Shifts of Trace Impurities: Industrially Preferred Solvents Used in Process and Green Chemistry. *Org. Process Res. Dev.* **2016**, *20* (3), 661–667. <https://doi.org/10.1021/acs.oprd.5b00417>.
- (58) Finney, W. F.; Wilson, E.; Callender, A.; Morris, M. D.; Beck, L. W. Reexamination of Hexafluorosilicate Hydrolysis by <sup>19</sup>F NMR and pH Measurement. *Environ. Sci. Technol.* **2006**, *40* (8), 2572–2577. <https://doi.org/10.1021/es052295s>.
- (59) Parimalam, B. S.; Lucht, B. L. Reduction Reactions of Electrolyte Salts for Lithium Ion Batteries: LiPF<sub>6</sub>, LiBF<sub>4</sub>, LiDFOB, LiBOB, and LiTFSI. *J. Electrochem. Soc.* **2018**, *165* (2), A251–A255. <https://doi.org/10.1149/2.0901802jes>.
- (60) Wiemers-Meyer, S.; Winter, M.; Nowak, S. Mechanistic Insights into Lithium Ion Battery Electrolyte Degradation – a Quantitative NMR Study. *Phys. Chem. Chem. Phys.* **2016**, *18* (38), 26595–26601. <https://doi.org/10.1039/C6CP05276B>.
- (61) Rice, C. L.; Whitehead, R. Electrokinetic Flow in a Narrow Cylindrical Capillary. *J. Phys. Chem.* **1965**, *69* (11), 4017–4024. <https://doi.org/10.1021/j100895a062>.

- (62) Biscombe, C. J. C. The Discovery of Electrokinetic Phenomena: Setting the Record Straight. *Angew. Chemie - Int. Ed.* **2017**, *56* (29), 8338–8340. <https://doi.org/10.1002/anie.201608536>.
- (63) Pivovar, B. S. An Overview of Electro-Osmosis in Fuel Cell Polymer Electrolytes. *Polymer (Guildf)*. **2006**, *47* (11), 4194–4202. <https://doi.org/10.1016/j.polymer.2006.02.071>.
- (64) Li, S. K.; Hao, J.; Liddell, M. *Electrotransport Across Membranes in Biological Media: Electrokinetic Theories and Applications in Drug Delivery*; Elsevier Inc., 2013. <https://doi.org/10.1016/B978-0-12-415824-5.00011-4>.
- (65) Harstad, R. K.; Johnson, A. C.; Weisenberger, M. M.; Bowser, M. T. Capillary Electrophoresis. *Anal. Chem.* **2016**, *88* (1), 299–319. <https://doi.org/10.1021/acs.analchem.5b04125>.
- (66) Jin, Y.; Kneusels, N. J. H.; Magusin, P. C. M. M.; Kim, G.; Castillo-Martínez, E.; Marbella, L. E.; Kerber, R. N.; Howe, D. J.; Paul, S.; Liu, T.; et al. Identifying the Structural Basis for the Increased Stability of the Solid Electrolyte Interphase Formed on Silicon with the Additive Fluoroethylene Carbonate. *J. Am. Chem. Soc.* **2017**, *139* (42), 14992–15004. <https://doi.org/10.1021/jacs.7b06834>.
- (67) Grossman, Robert, B. *The Art of Writing Reasonable Organic Reaction Mechanisms*; Springer US, 2004.
- (68) Clayden, J.; Greeves, N.; Warren, S. *Organic Chemistry*, second edi.; Oxford University Press, 2012.
- (69) Mahne, N.; Schafzahl, B.; Leypold, C.; Leypold, M.; Grumm, S.; Leitgeb, A.; Strohmeier, G. A.; Wilkening, M.; Fontaine, O.; Kramer, D.; et al. Singlet Oxygen Generation as a Major Cause for Parasitic Reactions during Cycling of Aprotic Lithium-Oxygen Batteries. *Nat. Energy* **2017**, *2* (5), 1–9. <https://doi.org/10.1038/nenergy.2017.36>.
- (70) Joiri, G.; Trotta, M. *Singlet Oxygen Applications in Biosciences and Nanoscience*; The Royal Society of Chemistry, 2016. <https://doi.org/10.1039/9781782622130-FP007>.
- (71) Zhuang, G. V.; Yang, H.; Ross, P. N.; Xu, K.; Jow, T. R. Lithium Methyl Carbonate as a Reaction Product of Metallic Lithium and Dimethyl Carbonate. *Electrochem. Solid-State Lett.* **2006**, *9* (2). <https://doi.org/10.1149/1.2142157>.
- (72) Sloop, S. E.; Kerr, J. B.; Kinoshita, K. The Role of Li-Ion Battery Electrolyte Reactivity in Performance Decline and Self-Discharge. **2003**, *121*, 330–337. [https://doi.org/10.1016/S0378-7753\(03\)00149-6](https://doi.org/10.1016/S0378-7753(03)00149-6).
- (73) Freiberg, A. T. S.; Sicklinger, J.; Solchenbach, S.; Gasteiger, H. A. Li<sub>2</sub>CO<sub>3</sub> Decomposition in Li-Ion Batteries Induced by the Electrochemical Oxidation of the Electrolyte and of Electrolyte Impurities. *Electrochim. Acta* **2020**, *346*, 136271. <https://doi.org/10.1016/j.electacta.2020.136271>.
- (74) Faenza, N. V.; Bruce, L.; Lebens-Higgins, Z. W.; Plitz, I.; Pereira, N.; Piper, L. F. J.; Amatucci, G. G. Growth of Ambient Induced Surface Impurity Species on Layered Positive Electrode Materials and Impact on Electrochemical Performance. *J. Electrochem. Soc.* **2017**, *164* (14), A3727–A3741. <https://doi.org/10.1149/2.0921714jes>.
- (75) Sloop, S. E.; Pugh, J. K.; Wang, S.; Kerr, J. B.; Kinoshita, K. Chemical Reactivity of PF<sub>5</sub> and LiPF<sub>6</sub> in Ethylene Carbonate/Dimethyl Carbonate Solutions. *Electrochem. Solid-State Lett.* **2001**, *4* (4), A42–A44. <https://doi.org/10.1149/1.1353158>.
- (76) Plakhotnyk, A. V.; Ernst, L.; Schmutzler, R. Hydrolysis in the System LiPF<sub>6</sub> — Propylene Carbonate — Dimethyl Carbonate — H<sub>2</sub>O. **2005**, *126*, 27–31. <https://doi.org/10.1016/j.jfluchem.2004.09.027>.
- (77) Nie, M.; Lucht, B. L. Role of Lithium Salt on Solid Electrolyte Interface (SEI) Formation and Structure in Lithium Ion Batteries. *J. Electrochem. Soc.* **2014**, *161* (6), A1001–A1006. <https://doi.org/10.1149/2.054406jes>.
- (78) Aurbach, D.; Daroux, M. L.; Faguy, P. W.; Yeager, E. Identification of Surface Films Formed on Lithium in Propylene Carbonate Solutions. *J. Electrochem. Soc.* **1987**, *134* (7), 1611. <https://doi.org/10.1149/1.2100722>.
- (79) Schechter, A.; Aurbach, D. X-Ray Photoelectron Spectroscopy Study of Surface Films Formed

- on Li Electrodes Freshly Prepared in Alkyl Carbonate Solutions. **1999**, *1* (13), 3334–3342. <https://doi.org/10.1021/la981048h>.
- (80) Xu, K. Electrolytes and Interphases in Li-Ion Batteries and Beyond. *Chem. Rev.* **2014**, *114* (23), 11503–11618. <https://doi.org/10.1021/cr500003w>.
- (81) Burns, J. C.; Kassam, A.; Sinha, N. N.; Downie, L. E.; Solnickova, L.; Way, B. M.; Dahn, J. R. Predicting and Extending the Lifetime of Li-Ion Batteries. *J. Electrochem. Soc.* **2013**, *160* (9), A1451–A1456. <https://doi.org/10.1149/2.060309jes>.
- (82) Dubarry, M.; Truchot, C.; Liaw, B. Y.; Gering, K.; Sazhin, S.; Jamison, D.; Michelbacher, C. Evaluation of Commercial Lithium-Ion Cells Based on Composite Positive Electrode for Plug-in Hybrid Electric Vehicle Applications. Part II. Degradation Mechanism under 2 C Cycle Aging. *J. Power Sources* **2011**, *196* (23), 10336–10343. <https://doi.org/10.1016/j.jpowsour.2011.08.078>.
- (83) Sen, R.; Goeppert, A.; Kar, S.; Prakash, G. K. S. Hydroxide Based Integrated CO<sub>2</sub> Capture from Air and Conversion to Methanol. *J. Am. Chem. Soc.* **2020**, *142* (10), 4544–4549. <https://doi.org/10.1021/jacs.9b12711>.
- (84) Kofron, W. G.; Wideman, L. G. Specific Synthesis and Selective Alkylation and Condensation of Monoesters of Substituted Succinic Acids. *J. Org. Chem.* **1972**, *37* (4), 555–559. <https://doi.org/10.1021/jo00969a006>.
- (85) Leskes, M.; Kim, G.; Liu, T.; Michan, A. L.; Aussenac, F.; Dorffer, P.; Paul, S.; Grey, C. P. Surface-Sensitive NMR Detection of the Solid Electrolyte Interphase Layer on Reduced Graphene Oxide. *J. Phys. Chem. Lett.* **2017**, *8* (5), 1078–1085. <https://doi.org/10.1021/acs.jpcllett.6b02590>.
- (86) Nixon, J. F.; Schmutzler, R. Phosphorus-31 Nuclear Magnetic Resonance Studies of Phosphorus-Fluorine Compounds. **1964**, *20* (1962).
- (87) Trincado, M.; Kühlein, K.; Grützmacher, H. Metal-Ligand Cooperation in the Catalytic Dehydrogenative Coupling (DHC) of Polyalcohols to Carboxylic Acid Derivatives. *Chem. - A Eur. J.* **2011**, *17* (42), 11905–11913. <https://doi.org/10.1002/chem.201101084>.
- (88) Rivlin, M.; Eliav, U.; Navon, G. NMR Studies of the Equilibria and Reaction Rates in Aqueous Solutions of Formaldehyde. *J. Phys. Chem. B* **2015**, *119* (12), 4479–4487. <https://doi.org/10.1021/jp513020y>.
- (89) Xu, M.; Xiao, A.; Yang, L.; Lucht, B. Novel Electrolyte for Lithium Ion Batteries: Lithium Tetrafluorooxalatophosphate (LiPF<sub>4</sub>C<sub>2</sub>O<sub>4</sub>). **2009**, 3–11. <https://doi.org/10.1149/1.3123122>.